



# Global high-resolution simulations of CO<sub>2</sub> and CH<sub>4</sub> using a NIES transport model to produce a priori concentrations for use in satellite data retrievals

T. Saeki<sup>1</sup>, R. Saito<sup>2</sup>, D. Belikov<sup>1,3</sup>, and S. Maksyutov<sup>1</sup>

<sup>1</sup>Center for Global Environmental Research, National Institute for Environmental Studies, Tsukuba, 305-8506, Japan

<sup>2</sup>Research Institute for Global Change, JAMSTEC, Yokohama, 236-0001, Japan

<sup>3</sup>Division for Polar Research, National Institute of Polar Research, Tachikawa, Tokyo 190-8518, Japan

*Correspondence to:* T. Saeki (saeki.tazu@nies.go.jp)

Received: 12 July 2012 – Published in Geosci. Model Dev. Discuss.: 6 August 2012

Revised: 18 December 2012 – Accepted: 18 December 2012 – Published: 25 January 2013

**Abstract.** The Greenhouse gases Observing SATellite (GOSAT) measures column-averaged dry air mole fractions of carbon dioxide and methane (XCO<sub>2</sub> and XCH<sub>4</sub>, respectively). Since the launch of GOSAT, model-simulated three-dimensional concentrations from a National Institute for Environmental Studies offline tracer Transport Model (NIES TM) have been used as a priori concentration data for operational near real-time retrievals of XCO<sub>2</sub> and XCH<sub>4</sub> from GOSAT short-wavelength infrared spectra at NIES. Although the choice of a priori profile has only a minor effect on retrieved XCO<sub>2</sub> or XCH<sub>4</sub>, a realistic simulation with minimal deviation from observed data is desirable. In this paper, we describe the newly developed version of NIES TM that has been adapted to provide global and near real-time concentrations of CO<sub>2</sub> and CH<sub>4</sub> using a high-resolution meteorological dataset, the Grid Point Value (GPV) prepared by the Japan Meteorological Agency. The spatial resolution of the NIES TM is set to 0.5° × 0.5° in the horizontal in order to utilise GPV data, which have a resolution of 0.5° × 0.5°, 21 pressure levels and a time interval of 3 h. GPV data are provided to the GOSAT processing system with a delay of several hours, and the near real-time model simulation produces a priori concentrations driven by diurnally varying meteorology. A priori variance–covariance matrices of CO<sub>2</sub> and CH<sub>4</sub> are also derived from the simulation outputs and observation-based reference data for each month of the year at a resolution of 0.5° × 0.5° and 21 pressure levels. Model performance is assessed by comparing simulation results with the GLOBALVIEW dataset and other

observational data. The overall root-mean-square differences between model predictions and GLOBALVIEW analysis are estimated to be 1.45 ppm and 12.52 ppb for CO<sub>2</sub> and CH<sub>4</sub>, respectively, and the seasonal correlation coefficients are 0.87 for CO<sub>2</sub> and 0.53 for CH<sub>4</sub>. The model showed good performance particularly at oceanic and free tropospheric sites. The high-resolution model also performs well in reproducing both the observed synoptic variations at some sites and stratospheric profiles over Japan. These results give us confidence that the performance of our GPV-forced high-resolution NIES TM is adequate for use in satellite retrievals.

## 1 Introduction

Global atmospheric transport models provide an effective means of quantifying the global cycle of long-lived atmospheric trace gases such as carbon dioxide (CO<sub>2</sub>) and methane (CH<sub>4</sub>). There is an increasing demand for high-resolution models that simulate global tracer transport over synoptic and sub-daily timescales to reproduce observed variations more accurately. For example, the Atmospheric Tracer Transport Model Intercomparison Project (TransCom) has initiated simulations of hourly and synoptic CO<sub>2</sub> concentration (Law et al., 2008; Patra et al., 2008), which will complement and make use of state-of-the-art measurements of greenhouse gases. In this TransCom continuous experiments, 25 transport models participated with two running at 0.5° × 0.5° resolution and the others running at

1° × 1° to 3.8° × 5.0° resolutions. Patra et al. (2008) concluded that increasing model horizontal resolution clearly improved the synoptic-scale variations in simulated CO<sub>2</sub>. Maksyutov et al. (2008) compared model CO<sub>2</sub> results at horizontal resolutions of 2.0°, 1.0°, 0.5° and 0.25° with continuous observations at a tower site in Japan and showed that increasing the model's horizontal resolution greatly improved the match with observations. However, most model simulations of these greenhouse gases are still carried out at horizontal resolutions of 1° × 1° ~ 3.75° × 2.5° (e.g., Allen et al., 2012; Saito et al., 2011; Patra et al., 2011).

Another demand for the high-resolution models stems from a new approach in which model-predicted CO<sub>2</sub> and CH<sub>4</sub> concentrations are used to give a priori concentrations for satellite spectroscopic data retrieval algorithms (e.g., Saitoh et al., 2009; Yoshida et al., 2011; O'Dell et al., 2012). Satellite observations cover most of the globe in several days to a few weeks, and retrievals based on satellite spectra require a priori concentrations of targeted gases. Global transport models can provide simulated a priori concentration profiles of those greenhouse gases in order to obtain optimal retrieval solutions and to physically interpret satellite-derived data. Instantaneous fields-of-view of satellite instruments are of the order of 10–100 km; e.g., 30 × 120 km<sup>2</sup> for the SCanning Imaging Absorption spectroMeter for Atmospheric CHartography (SCIAMACHY) (Buchwitz et al., 2005), and a nadir circular footprint of about 10.5 km diameter for the Greenhouse gases Observing SATellite (GOSAT) (Yoshida et al., 2011). For GOSAT, the retrieval precisions are estimated to be smaller than 3.5 ppm and 15 ppb for column-averaged dry air mole fractions of both carbon dioxide and methane (XCO<sub>2</sub> and XCH<sub>4</sub>), respectively (Yoshida et al., 2011). Furthermore, future satellites that observe greenhouse gases target higher precision with less bias. For example, the Orbiting Carbon Observatory-2 (OCO-2) is designed to retrieve XCO<sub>2</sub> theoretically with 1–2 ppm (0.3–0.5 %) precision for single-soundings with a small field-of-view with an area of 3 km<sup>2</sup> in nadir (Boesch et al., 2011). Therefore, much effort is currently being devoted to the development of global high-resolution transport models with less model error that meet the demands from satellite observations of greenhouse gases. For various applications of the retrieved data such as observations of strong CO<sub>2</sub> emissions by forest fire or volcano eruptions, users desire a near real-time data processing. To serve those needs, an operational retrieval in GOSAT data processing system is conducted at near real-time.

GOSAT is the first satellite to measure global distributions of XCO<sub>2</sub> and XCH<sub>4</sub> (Kuze et al., 2009; Yokota et al., 2009; Yoshida et al., 2011). At the National Institute for Environmental Studies (NIES), XCO<sub>2</sub> and XCH<sub>4</sub> are retrieved from the short-wavelength infrared (SWIR) spectra obtained by the Thermal And Near infrared Sensor for carbon Observation-Fourier Transform Spectrometer (TANSO-FTS) on board GOSAT. An optimal estimation method is used to retrieve XCO<sub>2</sub> and XCH<sub>4</sub> which minimises the cost

function

$$J(x) = [y - F(x)]^T S_e^{-1} [y - F(x)] + [x - x_a]^T S_a^{-1} [x - x_a] \quad (1)$$

where  $x$  is the state vector to be retrieved,  $y$  is the vector containing the observed spectrum,  $F(x)$  is the forward model that relates the state vector to the observed spectrum,  $S_e$  is the error covariance matrix of the observed spectrum,  $x_a$  is the a priori state of  $x$  and  $S_a$  is the a priori variance–covariance matrix (VCM) (Yokota et al., 2009; Yoshida et al., 2011). A priori state  $x_a$  includes a priori concentration profiles of CO<sub>2</sub> and CH<sub>4</sub>. The retrieved XCO<sub>2</sub> and XCH<sub>4</sub> at NIES are available after April 2009 at GOSAT User Interface Gateway (GUIG; <http://data.gosat.nies.go.jp/>).

As a priori concentrations for NIES XCO<sub>2</sub> and XCH<sub>4</sub> retrievals, we use simulated data from a NIES atmospheric tracer transport model (hereafter NIES TM) (Japan Aerospace Exploration Agency, National Institute for Environmental Studies, and Ministry of the Environment, 2011 (hereafter JAXA/NIES/MoE, 2011); Yoshida et al., 2011). The a priori VCMs,  $S_a$ , for CO<sub>2</sub> and CH<sub>4</sub> are derived from simulated NIES TM data and some reference data (Eguchi et al., 2010). The choice of a priori concentrations for satellite data retrievals is optional, and various a priori concentrations have been used to retrieve XCO<sub>2</sub> and XCH<sub>4</sub> from GOSAT SWIR spectra; e.g., constant a priori concentrations (Oshchepkov et al., 2011), monthly zonal means in 10° latitude bands for land and ocean from a forward model run (O'Dell et al., 2012), or model-simulated concentrations for the year 2007, 2008 (Butz et al., 2011) or 2009 that was extrapolated to 2010 (Schepers et al., 2012). However, as seen in Eq. (1), when the diagonal elements of  $S_a$  have small values, the a priori profiles largely constrain the retrieved results (e.g., Saitoh et al., 2009; Yoshida et al., 2011). We, thus, aim to reduce errors in a priori CO<sub>2</sub> and CH<sub>4</sub> concentrations for use in the NIES retrieval algorithm by using NIES TM at the relatively high horizontal resolution of 0.5° × 0.5°.

Distinctive feature of the NIES a priori concentrations is that they are created by NIES TM driven by a near real-time high-resolution meteorological dataset at a horizontal resolution of 0.5° × 0.5° and 21 pressure levels. As a result, real-time SWIR retrieval processing is made available to create XCO<sub>2</sub> and XCH<sub>4</sub> products at every observed day by using a priori concentrations that reflect daily meteorological variations at the observed days. Use of high-resolution meteorological data would be expected to allow smaller-scale phenomena to be represented in the model.

In this paper, we describe a newly developed high-resolution NIES TM designed to provide near real-time global three-dimensional concentration fields that reflect daily meteorological conditions for satellite retrieval algorithms, which is currently implemented in the GOSAT Level 2 retrieval system to derive XCO<sub>2</sub> and XCH<sub>4</sub> at NIES (Sect. 2). In Sect. 3, the simulated CO<sub>2</sub> and CH<sub>4</sub> concentrations are compared with an analysis of GLOBALVIEW-CO<sub>2</sub> (2009) and GLOBALVIEW-CH<sub>4</sub> (2009) data products

(hereafter GV-CO<sub>2</sub>, GV-CH<sub>4</sub>) and other observations to evaluate the model performance and investigate potential biases arising from the model simulation. Our conclusions follow in Sect. 4.

## 2 NIES transport model and numerical experiments

A NIES off-line global transport model (Maksyutov et al., 2008) has been used to simulate seasonal and spatial distributions of long-lived atmospheric constituents in the lower and mid-troposphere. The advection scheme of the model was semi-Lagrangian, and a mass fixer was adopted to conserve the total mass of tracers in the model for long-term simulation. The vertical mixing in the model was represented by cumulus convection and turbulent diffusion with explicitly parameterised Planetary Boundary Layer (PBL) physical processes. The details of the mass fixer, cumulus convection, and turbulent diffusion are described in Appendix A1–A3.

The earlier version of the NIES transport model (denoted NIES-99) was developed to simulate the seasonal cycles of long-lived tracer species at a relatively coarse horizontal resolution (2.5°–5.0° longitude–latitude), and to perform source–sink inversions of atmospheric CO<sub>2</sub> (e.g., Gurney et al., 2002, 2004; Patra et al., 2002, 2003, 2005a). Improvements to NIES-99 led to a recent development of the model (NIES-05), which has a higher horizontal resolution (tested on 2° × 2° to 0.25° × 0.25° in Maksyutov et al., 2008). NIES-05 was driven by the ECMWF 3-hourly PBL height data and the vertical resolution was enhanced to 47 levels (Appendix A4) for better resolution of the mixing processes in the boundary layer. For more details of NIES TM, see Maksyutov et al. (2008). NIES-05 was able to simulate observed diurnal-synoptic scale variability of tracers of interest, and participated in the TransCom hourly CO<sub>2</sub> experiment (Law et al., 2008; Patra et al., 2008). The original version of NIES-05 used meteorology datasets from NCEP final analyses (<http://dss.ucar.edu/datasets/ds083.2/>).

We have recently upgraded NIES-05 to utilise a high-resolution meteorological dataset, the Japan Meteorological Agency (JMA) Grid Point Values (GPV) product (Belikov et al., 2011). GPV/JMA data is created from JMA Global Spectral Model, which is operated for short- and medium-range forecasts covering the entire globe with TL959 resolution and 60 vertical levels from the surface to 0.1 hPa and assimilated by 4D-Var within a framework of JMA's numerical weather prediction system (<http://www.jma.go.jp/jma/en/Activities/nwp.html>; JMA, 2007). Original GPV data is provided at 0.5° × 0.5° horizontal resolution from the surface to 100 hPa and 1.0° × 1.0° above 100 hPa to 10 hPa (<http://www.jmbc.or.jp/hp/online/f-online0a.html>). For use in GOSAT project, GPV data is specially extended at a resolution of 0.5° × 0.5° up to 10 hPa. Since November 2007, the extended GPV has been supplied for the GOSAT Data Handling Facility (DHF; JAXA/NIES/MoE, 2011) at NIES

in near-real time (delay of several hours). The spatial resolution of the GOSAT version of the GPV dataset is 0.5° × 0.5° on 21 pressure levels (from 1000 to 10 hPa) and the time resolution is 3 h. We used both GPV objective analysis and forecasts. The GPV data and the ECMWF 3-hourly PBL height data in GRIB2 format are automatically converted to direct access binary for NIES TM input on DHF everyday. Data size is about 1.1 GB per one model day.

We employed the NIES-05 model driven by GPV data to simulate atmospheric CO<sub>2</sub> and CH<sub>4</sub> concentrations for use as a priori concentrations for GOSAT SWIR Level 2 processing at NIES. The horizontal resolution was 0.5° with 47 sigma vertical levels from the surface to 0.02 sigma, and simulated CO<sub>2</sub> and CH<sub>4</sub> concentrations were calculated for every observed day. The 21-level GPV data is interpolated to the model sigma levels just after reading GPV data every time step, and the model results are outputted every 3-h time after interpolating back to 21 pressure levels. Flux climatologies were prepared because no real-time fluxes were available. The climatological CO<sub>2</sub> flux dataset was prepared for the TransCom model inter-comparison studies (Gurney et al., 2004), which consisted of four components: (1) annual constant fossil fuel emissions with a spatial resolution of 0.5° × 0.5° (Brenkert, 1998); (2) three-hourly terrestrial biosphere flux obtained using the Carnegie–Ames–Stanford–Approach (CASA) model (Randerson et al., 1997; Law et al., 2008); (3) monthly varying ocean flux (Takahashi et al., 2002); and (4) monthly flux corrections obtained using the cyclostationary inversion approach (Gurney et al., 2004) with NIES-99. The annual total net flux of CO<sub>2</sub> to the atmosphere is 4.32 GtC. For CH<sub>4</sub>, we used the monthly varying flux for 2000 (575 Tg yr<sup>-1</sup>), as obtained from Patra et al. (2009). This CH<sub>4</sub> flux is based on the Emission Database for Global Atmospheric Research (EDGAR) version 32FT2000 (Olivier and Berdowski, 2001) for anthropogenic CH<sub>4</sub>, and on GISS emissions (Fung et al., 1991) for natural CH<sub>4</sub>. The chemical destruction of CH<sub>4</sub> by OH radicals was calculated based on climatological monthly mean OH radical concentrations (Spivakovsky et al., 2000) and a temperature-dependent rate constant. All these flux datasets were prepared at a spatial resolution of 1° × 1°, except for the CO<sub>2</sub> fossil fuel emission.

Stratospheric CO<sub>2</sub> and CH<sub>4</sub> variations are poorly understood due to a lack of precise observations over the globe. In addition, it is difficult to reproduce accurately transport and chemical processes in the stratosphere in NIES TM. This is a common problem in many transport models, where the model age of air in the stratosphere tends to be younger than that observed (Saito et al., 2011, and references therein). To reduce model biases in the stratosphere, the model stratospheric concentrations above the diagnosed tropopause are nudged towards the zonal-mean climatological concentrations based on observations. The tropopause in the model is determined from the gradient of potential temperature versus geopotential height at every model grid box at every

time step. Zonal-mean climatologies for CO<sub>2</sub> and CH<sub>4</sub> were prepared at 2.5° resolution for every month. CO<sub>2</sub> monthly climatological concentrations in the stratosphere were constructed using the Gap-filled Ensemble Climatology Mean (GECM; Saito et al., 2011). GECM is a three-dimensional daily CO<sub>2</sub> concentration generated by combining information from in situ measurements and multi-model means, carried out in the framework of the TransCom satellite experiment in which six models participated. The mean age of air in the GECM stratosphere has been corrected using in situ profiles of SF<sub>6</sub>. The latest version of GECM was used here with further corrections in the stratosphere; i.e., the vertical gradient in GECM CO<sub>2</sub> concentration at northern mid-latitudes from 30 hPa to 10 hPa was corrected to match CO<sub>2</sub> observations (Aoki et al., 2003; Engel et al., 2009). The climatological stratospheric CO<sub>2</sub> values were prepared from 2007 to 2015 with interannual variations for CO<sub>2</sub>. Extrapolation of the CO<sub>2</sub> climatology in time has been done by using average trend plus average seasonal cycle obtained from fitting GV-CO<sub>2</sub> data (Masarie and Tans, 1995) and by using stratospheric age of air (Saito et al., 2011). The stratospheric correction was about -0.5 ppm for XCO<sub>2</sub> in the northern mid-latitudes.

For CH<sub>4</sub>, monthly climatological values in the stratosphere were derived from satellite measurements by the Halogen Occultation Experiment (HALOE) (Russell et al., 1993), averaged over the period 1994–2005 to exclude the period of the Pinatubo eruption in 1991. HALOE provides a long time series of data, from October 1991 to November 2005 (Russell et al., 1993). Park et al. (1996) validated HALOE CH<sub>4</sub> data against the following correlative data from space-borne infrared spectroscopy: the Atmospheric Trace Molecule Spectroscopy Experiment; the MARK IV balloon-borne Fourier transform spectrometer; rocket-based cryogenic whole air sampler, balloon-borne laser in situ sensor; and the Kernforschungsanlage cryogenic whole air sampler. They concluded that the total error for the 0.3 to 50 hPa region was less than 15 % and the precision was better than 7 %. Thus, we consider the HALOE CH<sub>4</sub> dataset would be suitable for making climatological stratospheric CH<sub>4</sub> distributions. No clear trend had been seen in HALOE time series; thus, we repeatedly used the same monthly concentrations every year. This stratospheric correction was about -50 ppb for XCH<sub>4</sub> in the northern mid-latitudes.

The model was initialised with zonal-mean concentration fields on 1 January 2007 derived from GECM for CO<sub>2</sub> and GV-CH<sub>4</sub> (GLOBALVIEW-CH<sub>4</sub>, 2009) for CH<sub>4</sub>. As GPV data are only available after November 2007, the model for 2007 was forced with GPV 2008 data. CH<sub>4</sub> emissions were scaled to reproduce the 2007–2008 CH<sub>4</sub> trend at the South Pole (SPO) observed by the National Oceanic and Atmospheric Administration/Earth System Research Laboratory (NOAA/ESRL) in the WMO World Data Centre for Greenhouse Gases (WDCGG) database (<http://ds.data.jma.go.jp/gmd/wdcgg/wdcgg.html>). After 2 yr of spin-up with 2008

meteorological data, simulated concentrations at the model's southernmost grid box on 1 February 2009 were readjusted by offsets to the observed NOAA/ESRL CO<sub>2</sub> and CH<sub>4</sub> values at the South Pole from the WDCGG dataset. The model was then handed over for operational processing on the GOSAT DHF after February 2009. The JMA provides the GOSAT DHF with GPV data within a day and the near real-time model simulation has been performed for every observation day. The simulated CO<sub>2</sub> and CH<sub>4</sub> concentrations at 21 pressure levels have been provided as a priori concentrations to the GOSAT Level 2 data processing to retrieve XCO<sub>2</sub> and XCH<sub>4</sub> from SWIR spectra at NIES. Model integration time for one day for two tracers (CO<sub>2</sub> and CH<sub>4</sub>) is about 530 s by wall-clock time on a single CPU in the NIES Supercomputer System (NEC SX-8R/128M16).

To produce a priori VCMs of CO<sub>2</sub> and CH<sub>4</sub> in Eq. (1), we used the simulated concentrations for the year 2008, GV-CO<sub>2</sub>, GV-CH<sub>4</sub> and observational data. The details of the procedure to produce VCMs were described in Eguchi et al. (2010). In brief, the VCM was defined as the sum of the bias and noise components, where the bias was obtained from the difference in seasonal cycle between simulated results of NIES TM and GV data, and the noise components consist of synoptic and interannual variations. The synoptic term was calculated from NIES TM results and interannual variations are derived from GV datasets over a few decades. The VCMs of CO<sub>2</sub> and CH<sub>4</sub> were prepared at each grid box of 0.5° × 0.5°, on 21 pressure levels over the globe for each month. In this study, we modified the stratospheric part of the previous version of VCMs to obtain more realistic values; i.e., stratospheric CO<sub>2</sub> and CH<sub>4</sub> seasonal biases were set to the standard deviations of balloon-borne observations over Japan (Aoki et al., 2003; T. Nakazawa and S. Aoki, unpublished data, 2009) and HALOE, respectively. The resulting variances (diagonal elements) in the stratosphere were about 2–3 ppm<sup>2</sup> for CO<sub>2</sub> and about 500–10 000 ppb<sup>2</sup> for CH<sub>4</sub>. Figure 1 shows VCMs for CO<sub>2</sub> and CH<sub>4</sub> over Sanriku, Japan (141.8° E, 39.2° E) in August. The values of diagonal elements are large near the surface and decrease with height. They show positive correlations, particularly near the surface. The off-diagonal elements are positive around the diagonal elements, while there are negative correlations between some pressure levels. Correlations in the stratosphere (200–10 hPa) are close to zero, indicates a weak correlation between tropospheric and stratospheric time series.

### 3 Results and discussion

In the following subsections, we evaluate the model performance against the analysed data from GV-CO<sub>2</sub> and GV-CH<sub>4</sub>, and other observations. Annual mean and monthly biases of the simulated CO<sub>2</sub> and CH<sub>4</sub> are examined in Sects. 3.1 and 3.2, respectively. Synoptic variations that include annual trends are validated against some sites in the WDCGG

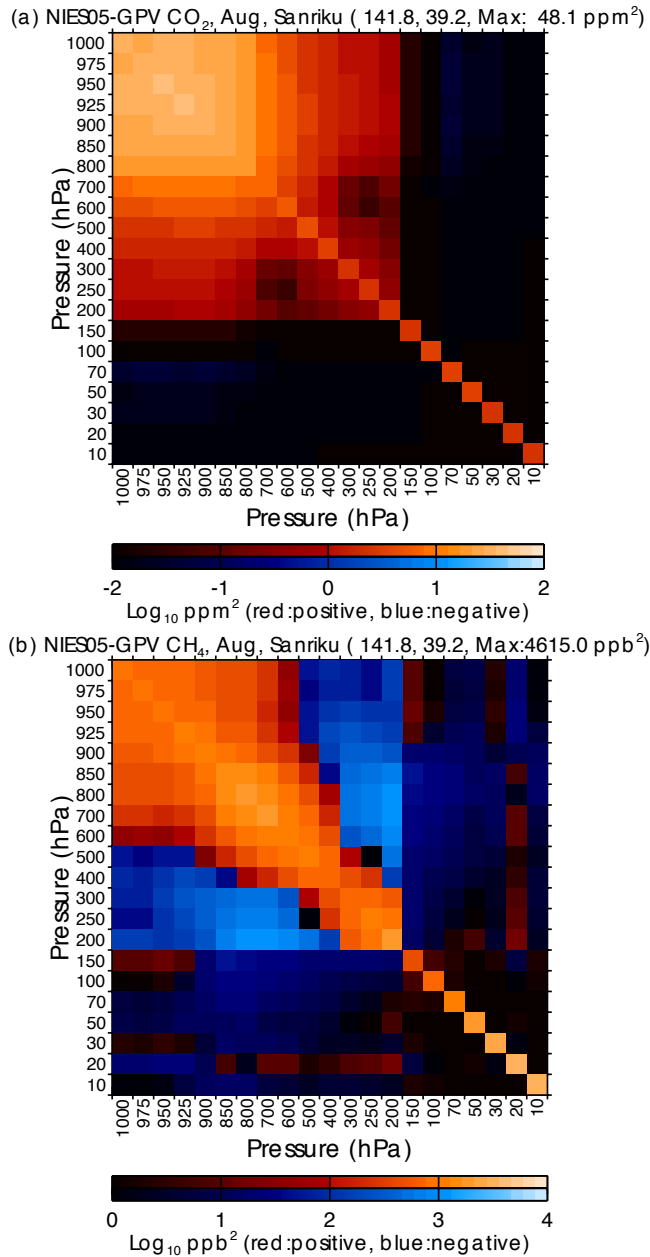


**Fig. 1.** A priori error variance–covariance matrices of (a) CO<sub>2</sub> and (b) CH<sub>4</sub> over Sanriku, Japan (39.2° N, 141.8° E) in August at 21 pressure levels from 1000 to 10 hPa. Colour scales are logarithmic, with ranges of 0.01–100 ppm<sup>2</sup> for CO<sub>2</sub> and 1–10 000 ppb<sup>2</sup> for CH<sub>4</sub>. Warm and cold colours indicate positive and negative correlations, respectively. Dark and light colours indicate small and large variance–covariance values, respectively.

dataset in Sect. 3.3. Balloon-borne observations in the stratosphere are used to validate the simulated vertical profiles in Sect. 3.4. Finally, the simulated surface CO<sub>2</sub> and CH<sub>4</sub> concentrations and their column-averaged dry air mole fractions are presented in Sect. 3.5. For all the comparisons, the nearest horizontal and vertical model grid box to the observation

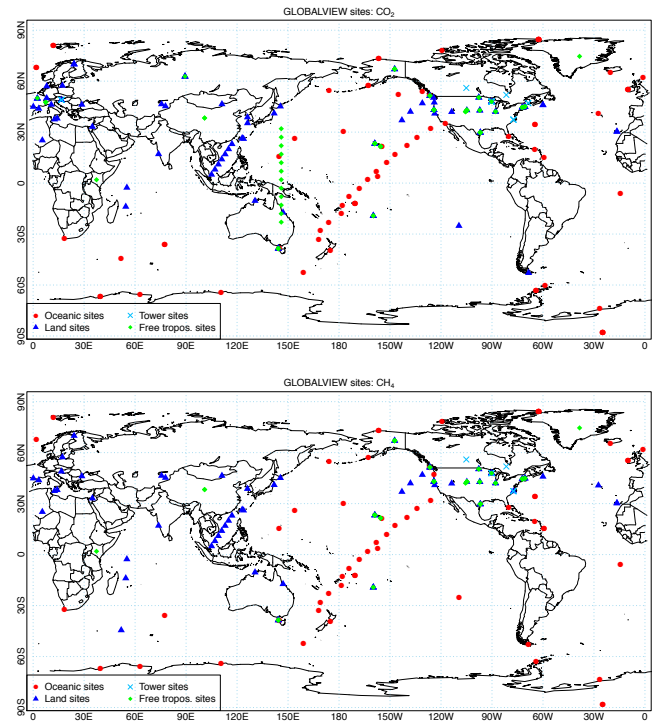


**Fig. 2.** GLOBALVIEW site locations used for the comparisons of CO<sub>2</sub> (top) and of CH<sub>4</sub> (bottom) for the year 2008. “Oceanic”; sites with marine-boundary-layer (MBL) marks in the GV dataset (gv\_table.co2 and gv\_table.ch4); “land”, sites below 3000 m which are neither MBL sites nor tower sites; “tower”, tower sites with sampling platform code “3” in GV file names; “free tropos.”, free troposphere sites located above 3000 m and marked as non-MBL sites, mostly airborne observational points.

location is selected. For comparison, simulations with lower horizontal resolution of 2.0° were performed with the same simulation set-up.

### 3.1 Comparison with observations: annual-mean biases

Annual means of simulated CO<sub>2</sub> and CH<sub>4</sub> concentrations are compared with those from GV analysis (GLOBALVIEW-CO<sub>2</sub>, 2009; GLOBALVIEW-CH<sub>4</sub>, 2009) for the year 2008 at 155 (CO<sub>2</sub>) and 123 (CH<sub>4</sub>) GV sites (Fig. 2) because no GV-CH<sub>4</sub> dataset is available for the years 2009 and 2010. Active sites in 2008 were used for comparisons. Annual mean biases of the simulated concentrations against GV analysis are shown in Table 1 and Fig. 3. Simulated results averaged over 13:00–16:00 LT were used for the comparison. In general, the annual mean model biases (difference between simulations and GV analysis) are found to be less than ~ 1 ppm for CO<sub>2</sub> and ~ 10 ppb for CH<sub>4</sub> at oceanic and Southern Hemisphere sites. The model also reproduces the GV pole-to-pole gradients very well for both CO<sub>2</sub> and CH<sub>4</sub>. In general, CO<sub>2</sub> might be expected to reproduce the GV data better than CH<sub>4</sub>

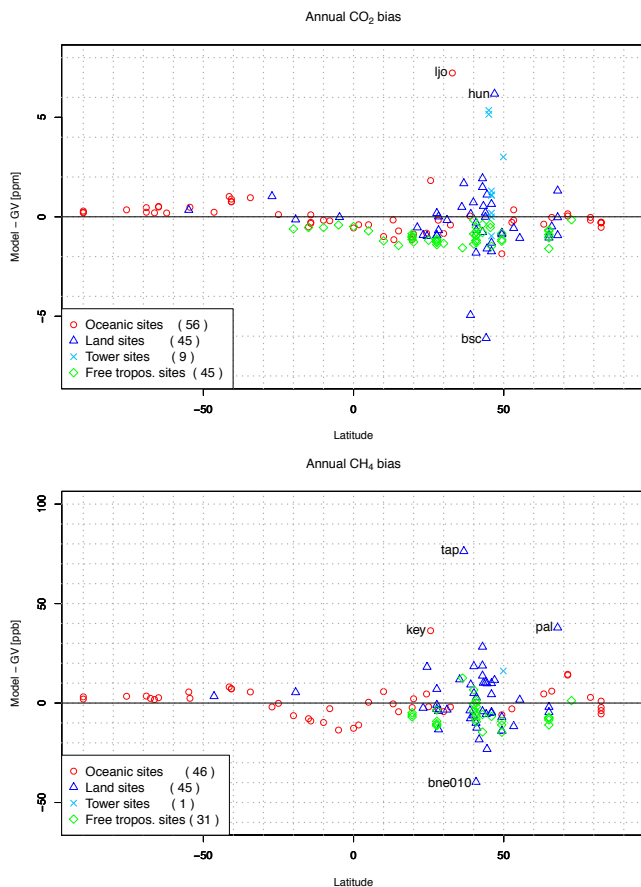


**Fig. 3.** Latitudinal distributions of differences in annual mean between the simulated and GV data for CO<sub>2</sub> (top) and CH<sub>4</sub> (bottom) at GV monitoring sites for the year 2008. The simulated results at 13:00–16:00 LT were used for the comparison. Letters in the plot represent the GV site code. Site types in the legend are the same as those defined in Fig. 2. Numbers in legend parentheses indicate the numbers of GV sites used for the analysis.

because the CO<sub>2</sub> climatological flux dataset includes flux correction by an inversion while CH<sub>4</sub> does not.

For CO<sub>2</sub>, the average annual mean bias and its standard deviation are  $-0.25 \pm 1.47$  ppm and RMSD of 1.45 ppm (Table 1), which shows good agreement with less than 1 % between the model prediction and the GV data at most of the sites. Some inland or near-continental sites show significant positive biases (e.g., LJO, La Jolla, California, 32.90° N, 117.30° W, 10 m a.s.l.; HUN, Hegyhatsal, Hungary, 46.95° N, 16.65° E, 248 m a.s.l.) or negative biases (BSC, Black Sea, Constanta, Romania, 44.17° N, 28.69° E, 3 m a.s.l.). LJO is located on the west coast of California and the GV dataset shows a clear seasonal cycle with small synoptic variations, which involve only differing oceanic air masses. However, a large point source with CO<sub>2</sub> 15 ppm higher than the surroundings appears on the model grid close to LJO, and it is clear that in the model LJO is affected by plumes from this point source. This may explain the large model–observation

mismatch at LJO. This might be caused by marine-only selection of LJO observations, climatological CO<sub>2</sub> fluxes and the high variability observed near source regions, which is not expected to be captured by global scale transport models. Even with the NIES TM 0.5° grids, such sub-grid scale dynamics could not be represented in the model. The BSC site is located in a coastal region of the Black Sea. Pérez-Landa et al. (2007a, b) studied the effect of regional and local meteorological conditions on CO<sub>2</sub> transport in the coastal area of Valencia, Spain and concluded that coastal circulation and strong local flux gradients introduced large biases against observations in a model. When a digital filter is applied to the BSC record in the GV data, large irregular seasonal variations of about  $-5$  to  $+5$  ppm are found, against regular seasonal peak-to-peak amplitudes of 14.8 ppm. BSC appears to be affected by local-scale circulation and/or local fluxes, and this may explain the failure of the model to reproduce BSC variations, as is the case also with HUN. The HUN site, a tall tower site, has the largest model–observation mismatch in the TransCom 3 seasonal experiment (Gurney et al., 2004). The model tends to overestimate GV data at some of the tower sites (e.g., AMT012 and AMT107, Argyle, Maine, United States, 45.03° N, 77.53° W, 50 m a.s.l.), mainly because of a failure to reproduce the large seasonal amplitudes and inter-annual variations, due to their location in areas affected by biogenic CO<sub>2</sub>, such as forest or inland plain, where it is difficult to fully represent the hourly climatological biogenic flux used in the model.

The simulated CH<sub>4</sub> mostly agree well with the GV data, with an average annual mean bias and standard deviation of  $-0.31 \pm 12.57$  ppb and RMSD of 12.52 ppb (Table 1). Significant positive or negative biases are found in Eurasia (TAP, Tae-ahn Peninsula, Republic of Korea, 36.73° N, 126.13° E, 20 m a.s.l.) and North America (BNE010, Beaver Crossing, Nebraska, airborne observation, 40.80° N, 97.18° W, 0–2000 m) with maximum 76 ppb and minimum  $-49$  ppb. TAP, on the western edge of Korea, is influenced by seasonally varying wind direction and local and remote CH<sub>4</sub> sources such as wetland (Dlugokencky et al., 1993), and this causes large interannual and seasonal variations, which the model finds difficult to reproduce. Located in the American Prairie, CH<sub>4</sub> at BNE010 exhibits scattered and large interannual variations and seasonal cycles, which is also difficult to reproduce by the model.

Satellite-retrieved XCO<sub>2</sub> is influenced by a priori profile (e.g., Rodgers, 1990; Connor et al., 2008), but variations of retrieved XCO<sub>2</sub> due to changes in the a priori profile appear to be relatively smaller for column observations (Reuter et al., 2011) such as GOSAT, SCIAMACHY and Total Carbon Column Observing Network (TCCON) data. According to validation results of GOSAT SWIR Level 2 XCO<sub>2</sub> and XCH<sub>4</sub> data (version 2.00) against surface FTS data from TCCON, average biases and 1 standard deviations were estimated to be  $-1.20 \pm 2.0$  ppm for XCO<sub>2</sub> and  $-7 \pm 12$  ppb for XCH<sub>4</sub> (NIES GOSAT project, 2012; Yoshida et al.,

**Table 1.** Statistics to show the model performance against GLOBALVIEW analyses of CO<sub>2</sub> and CH<sub>4</sub>: annual-mean biases and seasonal variations.

| Tracer          | Site type <sup>1</sup> | Number of sites | Annual mean                    |                   | Seasonal variation |                                       |                    |
|-----------------|------------------------|-----------------|--------------------------------|-------------------|--------------------|---------------------------------------|--------------------|
|                 |                        |                 | Biases and standard deviations | RMSD <sup>2</sup> | RSTD <sup>3</sup>  | Correlation coefficients <sup>4</sup> | CRMSD <sup>5</sup> |
| CO <sub>2</sub> | Oceanic                | 56              | -0.04 ± 1.16                   | 1.15              | 0.83               | 0.97                                  | 0.28               |
|                 | Land                   | 45              | -0.31 ± 1.74                   | 1.74              | 0.82               | 0.92                                  | 0.41               |
|                 | Tower                  | 9               | 1.80 ± 2.24                    | 2.77              | 0.66               | 0.65                                  | 0.76               |
|                 | Free tropos.           | 45              | -0.95 ± 0.38                   | 1.02              | 0.80               | 0.94                                  | 0.36               |
|                 | Total                  | 155             | -0.25 ± 1.47                   | 1.45              | 0.78               | 0.87                                  | 0.50               |
| CH <sub>4</sub> | Oceanic                | 46              | 0.72 ± 8.20                    | 8.15              | 1.14               | 0.70                                  | 0.84               |
|                 | Land                   | 45              | 2.05 ± 17.66                   | 17.58             | 0.43               | 0.43                                  | 1.21               |
|                 | Tower                  | 1               | 16.13                          | 16.13             | 1.58               | 0.025                                 | 1.83               |
|                 | Free tropos.           | 31              | -5.79 ± 5.86                   | 8.17              | 1.07               | 0.63                                  | 0.89               |
|                 | Total                  | 123             | -0.31 ± 12.57                  | 12.52             | 1.20               | 0.53                                  | 1.08               |

<sup>1</sup> Site types: the same as those defined in Fig. 2. <sup>2</sup> Root-mean-square differences (RMSD). <sup>3</sup> Ratio of standard deviation (SD), which is calculated by dividing the model SD by the observed SD. <sup>4</sup> Pearson's correlation coefficient. <sup>5</sup> Centred pattern root-mean-square differences (CRMSD), which is a measure of the distance between model and observation.

2013). The annual mean biases of the model against GV sites obtained in this study ( $-0.25 \pm 1.47$  ppm for CO<sub>2</sub> and  $-0.31 \pm 12.57$  ppb for CH<sub>4</sub>) are small enough. For in-land area where larger biases were found at some sites, the a priori VCMs are relatively larger than those for oceanic area because model seasonal biases were taken into account in the VCMs (see Sect. 2 or Eguchi et al., 2010). Thus, the model performance is thought to be good enough to be used for a priori concentrations for GOSAT Level 2 retrievals.

### 3.2 Comparison with observations: monthly biases

To assess the ability of the model to reproduce seasonal variations, the simulated monthly mean concentrations of CO<sub>2</sub> and CH<sub>4</sub> for the year 2008 were compared with the analysed seasonal cycles at GV sites (Fig. 4). Analysed seasonal cycles at GV sites were taken from “seas” files stored in the dataset. The simulated results were detrended and monthly means of 13:00–16:00 LT concentrations used for the comparison.

The characteristics of the observed seasonal variability at oceanic sites and free troposphere sites (above 3000 m altitude) are generally reproduced fairly well by the model for both CO<sub>2</sub> and CH<sub>4</sub>, but relatively large biases are found at tower sites and some of the land sites. Standard deviations over all GV sites are 1.47 ppm for CO<sub>2</sub> and 12.57 ppb for CH<sub>4</sub>. Large seasonal biases over 10 ppm in CO<sub>2</sub> are seen at tower sites in mid-northern latitudes such as AMT and LEF (Park Falls, Wisconsin, United States, 45.95° N, 90.27° W, 472 m a.s.l.); both sites provide continuous measurements and are located near forested areas on the eastern coast of the United States. Seasonal biases at AMT and ITN show that the model seasonal amplitudes are smaller than those in

the GV analysis; i.e., the model overestimates the observed summer minima in July and August and underestimates winter maxima. At continental sites with quasi-continuous measurements such as the towers, both the regional-local transport and daily flux variability, including temporal resolution of the biospheric fluxes, are found to be important in simulating such high-frequency CO<sub>2</sub> behaviour (Geels et al., 2004, 2007; Patra et al., 2008; Wang et al., 2007). Patra et al. (2008) also found that at lower levels some models overestimated the magnitudes of synoptic variations at high-frequency observational sites at tall towers such as LEF. These small-scale phenomena may influence model–observation mismatches at tower sites even though the comparisons are on a monthly basis. Except for such tower sites and inland sites, the model succeeds in capturing the GV seasonal variations with biases smaller than 5 ppm at most sites and for most months.

For CH<sub>4</sub>, the monthly model biases fall within about 20 ppb at oceanic and free troposphere sites (mostly airborne observational points). In particular, there appear to be no significant monthly model biases in the Southern Hemisphere. The seasonal biases for oceanic sites increase as moving northward with a maximum bias about 30 ppb. At continental sites such as TAP (Korea) and BSC (Romania), the agreement was poorer, mainly due to the influences of strong sources located near the sites and extreme climate conditions such as a strong inversion layer in a cold winter.

Statistics of monthly CO<sub>2</sub> and CH<sub>4</sub> biases against the GV analysis for the year 2008 are shown in Table 1 and Fig. 5. The overall correlation coefficients between the observed and modelled seasonal patterns at the GV sites are 0.87 for CO<sub>2</sub> and 0.53 for CH<sub>4</sub>, which shows a high degree of consistency between the model and the GV analyses. High correlations



(COI; 43.15° N, 145.50° E, 96 m a.s.l.). CO<sub>2</sub> and CH<sub>4</sub> data at MLO and SPO were provided by NOAA/ESRL in the WDCGG dataset (Dlugokencky, 2012a, b; Thoning, 2012a, b). Daily CO<sub>2</sub> data at HAT and COI were available from the Greenhouse Gases Trend Update (<http://db.cger.nies.go.jp/g3db/ggtu/index.html>) operated by the Center for Global Environmental Research (CGER), NIES. CH<sub>4</sub> data at HAT are hourly data (Tohjima et al., 2002, 2010; T. Tohjima, unpublished data, 2011). CH<sub>4</sub> observations at SPO are discrete observations and the other observations are continuous measurements. The continuous data and the 3-hourly model output were daily averaged based on local time for each site. As described in Sect. 2, GPV data are only available after December 2007, so the year 2008 meteorological data were used from January to November 2007 for the simulation.

Comparisons with continuous measurements of CO<sub>2</sub> and CH<sub>4</sub> show that the model was able to capture the observed synoptic and seasonal variations at each monitoring station (Fig. 6). Simulated CO<sub>2</sub> at MLO shows good agreement with the observed CO<sub>2</sub> though the model underestimates the observed spring maxima in 2008 and 2010, while simulated CH<sub>4</sub> at MLO slightly underestimates the observed CH<sub>4</sub> by about 20 ppb after 2009. MLO is remote from the large source regions, which are mainly on land and transport is, therefore, a dominant factor for CO<sub>2</sub> variability. Unlike CO<sub>2</sub>, CH<sub>4</sub> reacts with OH radicals during transport, which affects CH<sub>4</sub> variability. The interannual variability of atmospheric circulation is also important for the growth rate at MLO because transport determines the area the air mass come from, such as boreal Asia, the North Pacific or the tropical Atlantic (Higuchi et al., 2002; Patra et al., 2005b). In this mean, the model transport reproduces the overall features of observed CO<sub>2</sub> and CH<sub>4</sub> at MLO, but the use of climatological fluxes in this study gives some discrepancies. At SPO, another remote site away from strong source regions, the observed CO<sub>2</sub> has very small seasonal variations. A gap in the simulated CO<sub>2</sub> at the end of January 2009 is due to the offset correction described in Sect. 2. Differences between the model and the observed small variations in the first half of 2010 are slightly large at 2 ppm, which might be due to climatological CO<sub>2</sub> fluxes and model transport error. Otherwise, the simulated CO<sub>2</sub> trend generally matches the observed one. In spite of the OH sink, the simulated CH<sub>4</sub> reproduces the observed CH<sub>4</sub> at SPO very well except for the second half of 2010, where there occurs a large increase in observed CH<sub>4</sub>.

HAT is an island located on the East-Asian continental margin and is influenced by air masses transported from the Pacific Ocean in summer and from the continent in winter (Tohjima et al., 2002, 2010). Larger seasonal amplitudes and larger synoptic events are, therefore, observed here, relative to the background sites MLO and SPO. Though the CO<sub>2</sub> fluxes in the model are climatological, the model can simulate the observed seasonal pattern and occasional synoptic events such as the low concentrations in August 2008 and 2009. High-CO<sub>2</sub> events in winter are difficult to represent

perfectly in the model, possibly due to the transport of CO<sub>2</sub> from continental urban areas, but the model successfully simulates observed spring maxima. CH<sub>4</sub> at HAT is also well reproduced by the model; i.e., the model shows a clear seasonal pattern of summer and winter air mass exchanges. The model sometimes even captures sudden summer high CH<sub>4</sub>. Basically HAT is covered by oceanic air mass and the CH<sub>4</sub> fluxes in the model are climatological; thus, these high-CH<sub>4</sub> events are thought to be CH<sub>4</sub> transported from continental CH<sub>4</sub> source regions.

COI is located in the eastern part of Hokkaido, Japan. The monitoring station fronts onto the northwest Pacific Ocean and is influenced generally by northwesterly winds in winter and southwesterly winds in summer (Tohjima et al., 2002). Reflecting seasonal variations of seasonally varying air mass from Japan and East Asia, CO<sub>2</sub> concentration at COI shows larger seasonal variation than that at HAT. The model captures overall features of CO<sub>2</sub> trend and seasonal variations at COI.

Table 2 lists the statistics (ratio of standard deviations, correlation coefficients, overall biases, centred pattern root-mean-square differences) between daily averaged modelled and observed CO<sub>2</sub> and CH<sub>4</sub> at the three sites. As described above, only CH<sub>4</sub> at SPO is discrete data and the modelled CH<sub>4</sub> is taken from the same date and time as the observation. The statistics suggest that the model can simulate the observed daily CO<sub>2</sub> and CH<sub>4</sub> variations fairly well with a correlation coefficient ( $r$ ) > 0.8 at the four sites, except for CH<sub>4</sub> at MLO ( $r = 0.59$ ). The calculated RSTDs are nearly 1 and overall biases are less than 1 ppm for CO<sub>2</sub> and 10 ppb for CH<sub>4</sub>. CRMSDs are also below 1, indicating that the model performs reasonably well. Though the analytical period is almost the same for COI and HAT analysis, the model performance at COI site is relatively worse than that at HAT site because COI site is more affected by land vegetation than HAT site, and this makes it difficult to reproduce the COI observations.

Figure 7 illustrates synoptic-scale variations of CO<sub>2</sub> and CH<sub>4</sub> at HAT and CO<sub>2</sub> at COI. Synoptic variations were de-seasonalised and detrended variations which were extracted from the observed and simulated time series (Fig. 6) by using a digital filter technique (Nakazawa et al., 1997). The synoptic variation in CO<sub>2</sub> at HAT is larger in summer than in winter due to air mass from East Asia. CH<sub>4</sub> at HAT observed numerous peaks throughout the year, which reaches at about 150 ppb. CO<sub>2</sub> at COI has large synoptic variability in summer time. Table 3 lists statistics of the model performances of 0.5° and 2.0° simulations against the observed synoptic variations. The ratio of standard deviations range from 0.73 to 1.10, and the difference between 0.5° and 2.0° simulations are small. At COI site where is closer to land vegetation than HAT site, RSTD for 0.5° simulation is larger than that for 2.0° simulation, which can be attributed to surface fluxes and/or local transport biases. The correlation coefficients for 0.5° simulation show better performance than those for 2.0°

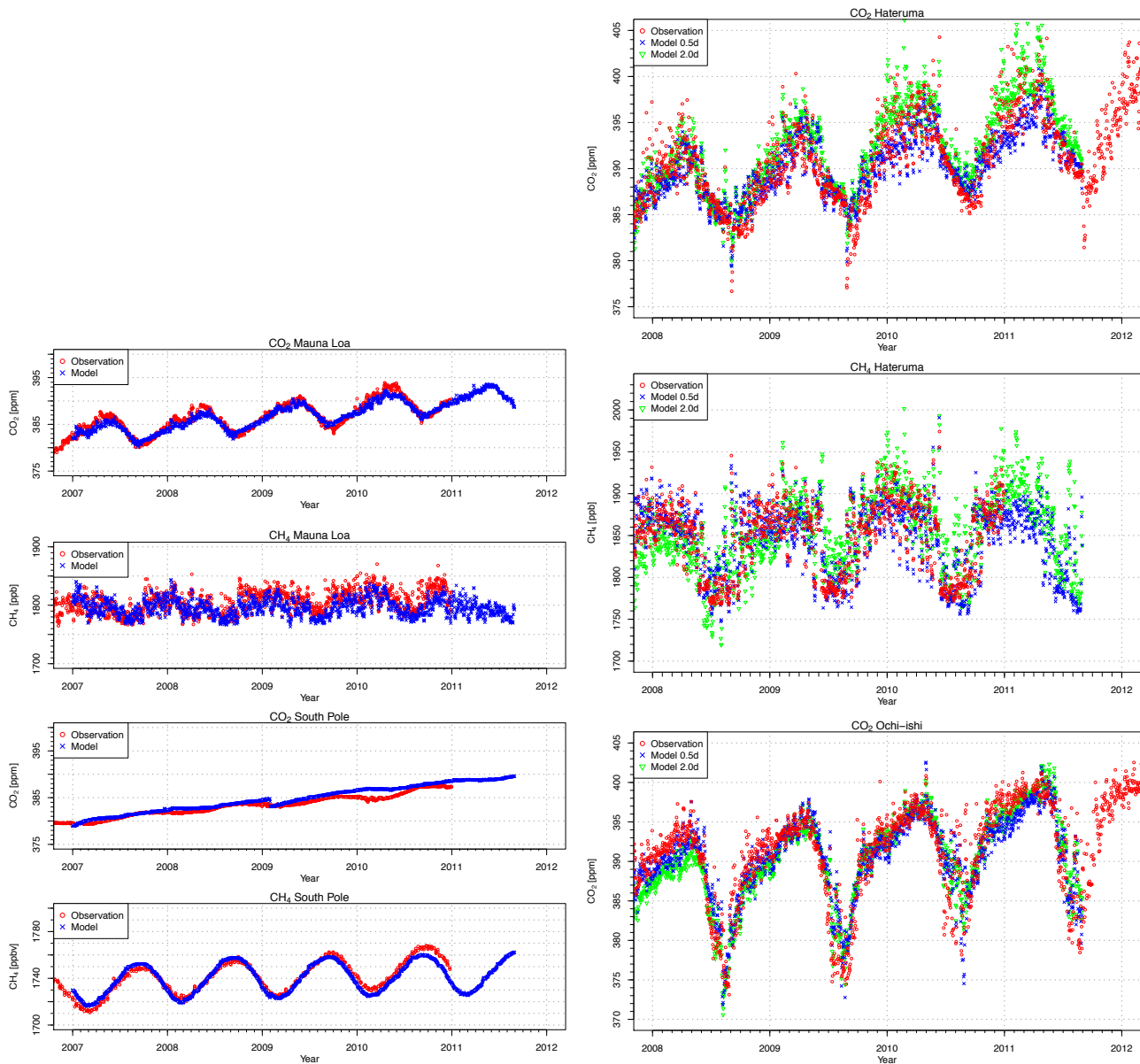


**Fig. 6.** Observed and simulated time series of daily mean CO<sub>2</sub> and CH<sub>4</sub> concentrations at Mauna Loa, South Pole and Hateruma sites, and CO<sub>2</sub> concentration at Ochi-ishi sites. CH<sub>4</sub> observations at South Pole are discrete data and are plotted directly; quasi-continuous data at the other sites and 3-hourly model output are daily averages. “0.5d” and “2.0d” in legends for Hateruma and Ochi-ishi sites indicate 0.5-degree simulation and 2.0-degree simulation, respectively. A gap in the simulated CO<sub>2</sub> at SPO at the end of January 2009 is due to the offset correction (see text).

simulation. In general, high-resolution model correlates better with the observations, though RSTD is slightly worse than the lower-resolution model in some cases.

### 3.4 Comparison with observations: stratospheric profiles

There are few periodical high-precision observations of CO<sub>2</sub> and CH<sub>4</sub> in the stratosphere, but observations are made over Japan about once a year using a balloon-borne cryogenic

sampler operated by Tohoku University, Japan (Nakazawa et al., 2002; Aoki et al., 2003). In this study, we compare the simulated stratospheric profiles of CO<sub>2</sub> and CH<sub>4</sub> with the observed mean profiles from the balloon-borne data over Japan. The observed mean profiles and their standard deviations are obtained as follows: first the observed tracer concentrations over Sanriku (39.2° N, 141.8° E), Japan from 1985 to 2007 are averaged in each of five height bins: below 15 km, 15–20 km, 20–25 km, 25–30 km, above 30 km; then the concentrations at the highest level are shifted to match observations

**Table 2.** Statistics to show the model performance against continuous measurements for daily-mean CO<sub>2</sub> and CH<sub>4</sub> at HAT (Hateruma), Cape Ochi-ishi (COI), MLO (Mauna Loa) and SPO (South Pole). Observed CH<sub>4</sub> data at SPO are discrete data and the simulated results corresponding to the measurement date are used for the comparisons. Statistics are defined as in Table 1.

| Tracers         | Site | Time interval comparisons | Period of comparisons  | Number of data | RSTD | Correlation coefficients | Overall bias | CRMSD |
|-----------------|------|---------------------------|------------------------|----------------|------|--------------------------|--------------|-------|
| CO <sub>2</sub> | HAT  | Daily                     | 1 Jan 2007–30 Aug 2011 | 1638           | 0.82 | 0.90                     | −0.29        | 0.44  |
|                 | COI  | Daily                     | 1 Jan 2007–31 Aug 2011 | 1644           | 0.59 | 0.73                     | −40.44       | 0.70  |
|                 | MLO  | Daily                     | 1 Jan 2007–31 Dec 2010 | 1351           | 0.88 | 0.96                     | −0.41        | 0.28  |
|                 | SPO  | Daily                     | 1 Jan 2007–31 Dec 2010 | 1439           | 1.12 | 0.98                     | 0.73         | 0.25  |
| CH <sub>4</sub> | HAT  | Daily                     | 1 Jan 2007–31 Dec 2010 | 1421           | 0.95 | 0.83                     | 2.44         | 0.57  |
|                 | MLO  | Daily                     | 1 Jan 2007–31 Dec 2010 | 1377           | 0.82 | 0.59                     | −9.83        | 0.84  |
|                 | SPO  | Event                     | 1 Jan 2007–31 Dec 2010 | 191            | 0.92 | 0.96                     | −1.19        | 0.30  |

**Table 3.** Correlation coefficients and Ratio of standard deviation between synoptic variations, that is, detrended and deseasonalised variations in observed and simulated CO<sub>2</sub> and CH<sub>4</sub> concentrations at HAT (Hateruma), Cape Ochi-ishi (COI). “0.5°” and “2.0°” indicate 0.5-degree simulation and 2.0-degree simulation, respectively. Statistics are defined as in Table 1.

| Tracers         | Site | Time interval of comparisons | Period of comparisons  | Number of data | Correlation coefficient |      | RSTD |      |
|-----------------|------|------------------------------|------------------------|----------------|-------------------------|------|------|------|
|                 |      |                              |                        |                | 0.5°                    | 2.0° | 0.5° | 2.0° |
| CO <sub>2</sub> | HAT  | Daily                        | 1 Jan 2008–31 Dec 2010 | 1064           | 0.72                    | 0.41 | 0.73 | 0.82 |
|                 | COI  | Daily                        | 1 Jan 2008–31 Dec 2010 | 1644           | 0.62                    | 0.55 | 0.85 | 0.71 |
| CH <sub>4</sub> | HAT  | Daily                        | 1 Jan 2008–31 Dec 2010 | 1057           | 0.85                    | 0.56 | 1.08 | 1.10 |

carried out on 22 August 2012 over Taiki-cho (42.48° N, 143.42° E), Japan (Nakazawa et al., 2002; Aoki et al., 2003; T. Nakazawa and S. Aoki, unpublished data, 2010). The simulated profiles on the same day over Sanriku are compared with the averaged observed profiles (Fig. 8). The simulated profile of CO<sub>2</sub> (corrected by age of air in the stratosphere, Sect. 2) is a close match to the observations with no bias on the day, and the difference between simulated and observed CO<sub>2</sub> profiles is within the standard deviation of the observed CO<sub>2</sub>. The simulated CH<sub>4</sub> profile also shows very good agreement with the observed profiles within the observed standard deviation, though the simulated profile tends to be smaller than the observed one at a height of about 100–20 hPa. Recently, De Mazière et al. (2008) compared CH<sub>4</sub> profiles from the Atmospheric Chemistry Experiment–Fourier Transform Spectrometer (ACE–FTS) launched on August 2003 with those from HALOE. They found both instruments showed similar average profiles and variability from 15 km to 70 km, and though ACE–FTS showed slightly higher biases compared with HALOE, they concluded that their differences were in the order of 5 % below 35 km (the target region of the present study) and were not significant because the error bars overlapped.

Though the model–observation comparison is for only one profile due to the lack of stratospheric observations, the agreement between the simulated and observed profiles shows that nudging the model stratosphere to the climatology

field of CO<sub>2</sub> (corrected by age of air) and CH<sub>4</sub> (HALOE) works quite well with no bias on the observed day or within the observed standard deviations.

### 3.5 Global distributions

Overall, the model successfully reproduces the observed variations of CO<sub>2</sub> and CH<sub>4</sub> as described in the previous sections. In this section, we present the latitude–longitude distributions for both the model surface level and the column-averaged dry air mole fractions. Column-averaged dry air mole fractions, XCO<sub>2</sub>, was obtained by weighing the concentration in each layer by the air mass in that layer from the model output at 21 pressure levels; thus,

$$XCO_2 = \sum_{n=L}^{21} CO_2^n \times \frac{\Delta P_n}{P_{\text{srf}}}, \quad (2)$$

where CO<sub>2</sub><sup>n</sup> is the CO<sub>2</sub> concentration in layer *n* defined at a layer centre in the pressure level coordinate, *L* is the lowest level of the grid (surface level), *P*<sub>srf</sub> is surface pressure and Δ*P*<sub>*n*</sub> is the thickness of layer *n* in pressure. XCH<sub>4</sub> is calculated in the same way.

The temporal and spatial patterns of CO<sub>2</sub> and CH<sub>4</sub> are primarily governed by seasonal cycles of the sources, sinks and atmospheric transport. Column abundances are also sensitive to changes in surface pressure and the tropopause height (e.g., Washenfelder et al., 2003). Figures 9 and 10 show the

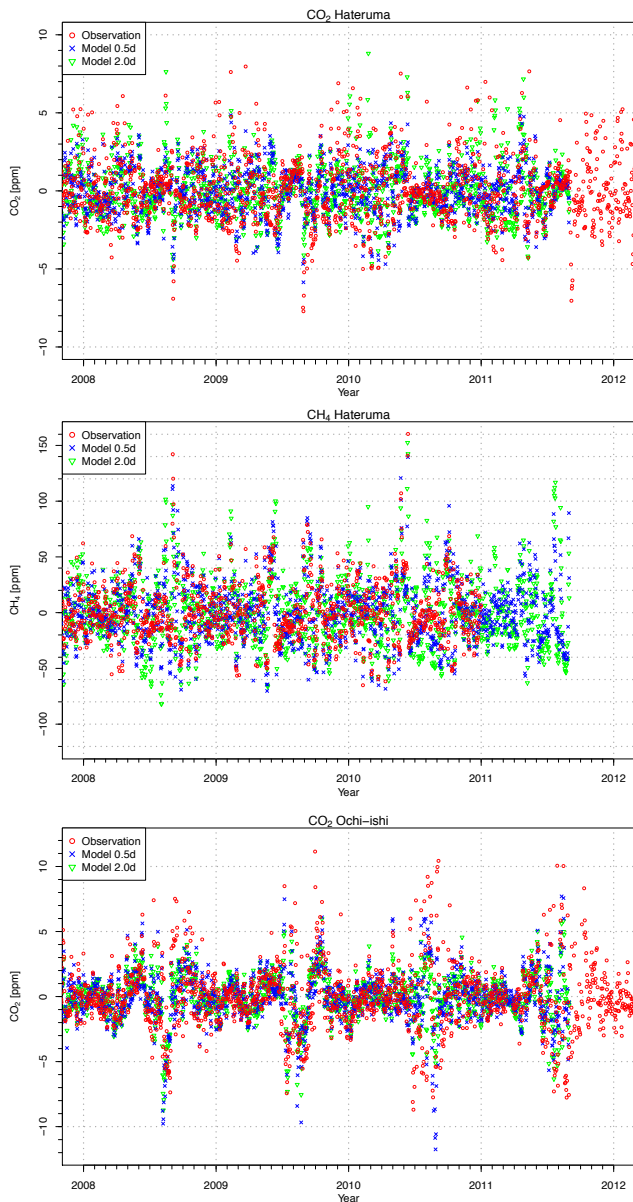


**Fig. 7.** Synoptic variations in observed and simulated time series of daily mean CO<sub>2</sub> and CH<sub>4</sub> concentrations at Hateruma site and CO<sub>2</sub> concentration at Ochi-iishi site. “0.5d” and “2.0d” in legends indicate 0.5-degree simulation and 2.0-degree simulation, respectively.

simulated surface CO<sub>2</sub> and CH<sub>4</sub> concentrations, column CO<sub>2</sub> and CH<sub>4</sub>, and their differences for January and July 2010 all at 13:00 LT, almost the same time as the GOSAT orbit descending node around 12:48 LT (Yoshida et al., 2011). Surface CO<sub>2</sub> concentrations in January are highest over high-emission areas such as Europe, northeast America, Siberia and Asia in the northern mid and high latitudes, and also over the equatorial regions (Africa, East South Asia, South America). Strong sinks in July are found in mid and high latitudes in Siberia and North America due to photosynthesis

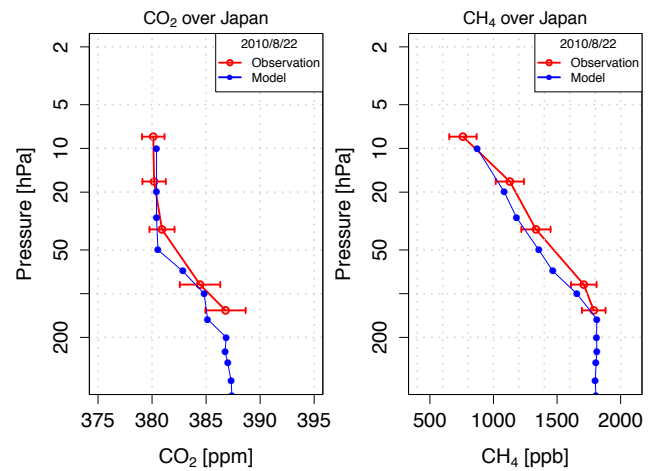


**Fig. 8.** Vertical profiles of CO<sub>2</sub> (left) and CH<sub>4</sub> (right) in the stratosphere over Japan. The blue lines indicate NIES TM simulated data on 22 August 2010. The red lines are observed average profiles and their standard deviations derived from balloon-borne measurements over Sanriku, Japan (39.2° N, 141.8° E).

by land biomass in summer. Compared with the continental regions, the marine boundary layers exhibit low concentrations because of the absence of strong sources. In the Southern Hemisphere, the CO<sub>2</sub> concentrations are relatively homogenous, except for some limited continental areas such as South America. XCO<sub>2</sub> has less variation than surface CO<sub>2</sub>, as expected. Strong sources over China, India and Equatorial Africa and a strong sink in Siberia are still recognisable in XCO<sub>2</sub>, particularly in July. Their difference (XCO<sub>2</sub> – surface CO<sub>2</sub>) is generally smaller in equatorial regions due to the high tropopause height, and larger in northern high latitudes due to strong sources/sinks, low tropopause height and PBL height. In July their difference is positive over mid and high northern latitudes due to large sinks at the surface. Nakazawa et al. (1993) found that the observed seasonal variation of CO<sub>2</sub> concentration showed a phase delay of about 1 month between the lower and upper troposphere by using long-term airborne observations over Japan. This fact supports the positive difference between XCO<sub>2</sub> and surface CO<sub>2</sub> over strong sink regions in mid and high northern latitudes.

High-CH<sub>4</sub> regions are simulated at the surface over land both in January and July, and CH<sub>4</sub> is higher in the Northern Hemisphere than in the Southern Hemisphere throughout the year due to large CH<sub>4</sub> emission in the Northern Hemisphere. XCH<sub>4</sub> exhibits the same trend as surface CH<sub>4</sub>: relatively high in the Northern Hemisphere and low in the Southern Hemisphere. High-XCH<sub>4</sub> regions, which appear over south and eastern Asia and equatorial Africa, are associated with deep convection over these areas. Xiong et al. (2009) found a high-CH<sub>4</sub> plume over south Asia in the middle to upper troposphere associated with the monsoon season during July–September. These convective flows transport surface CH<sub>4</sub> to

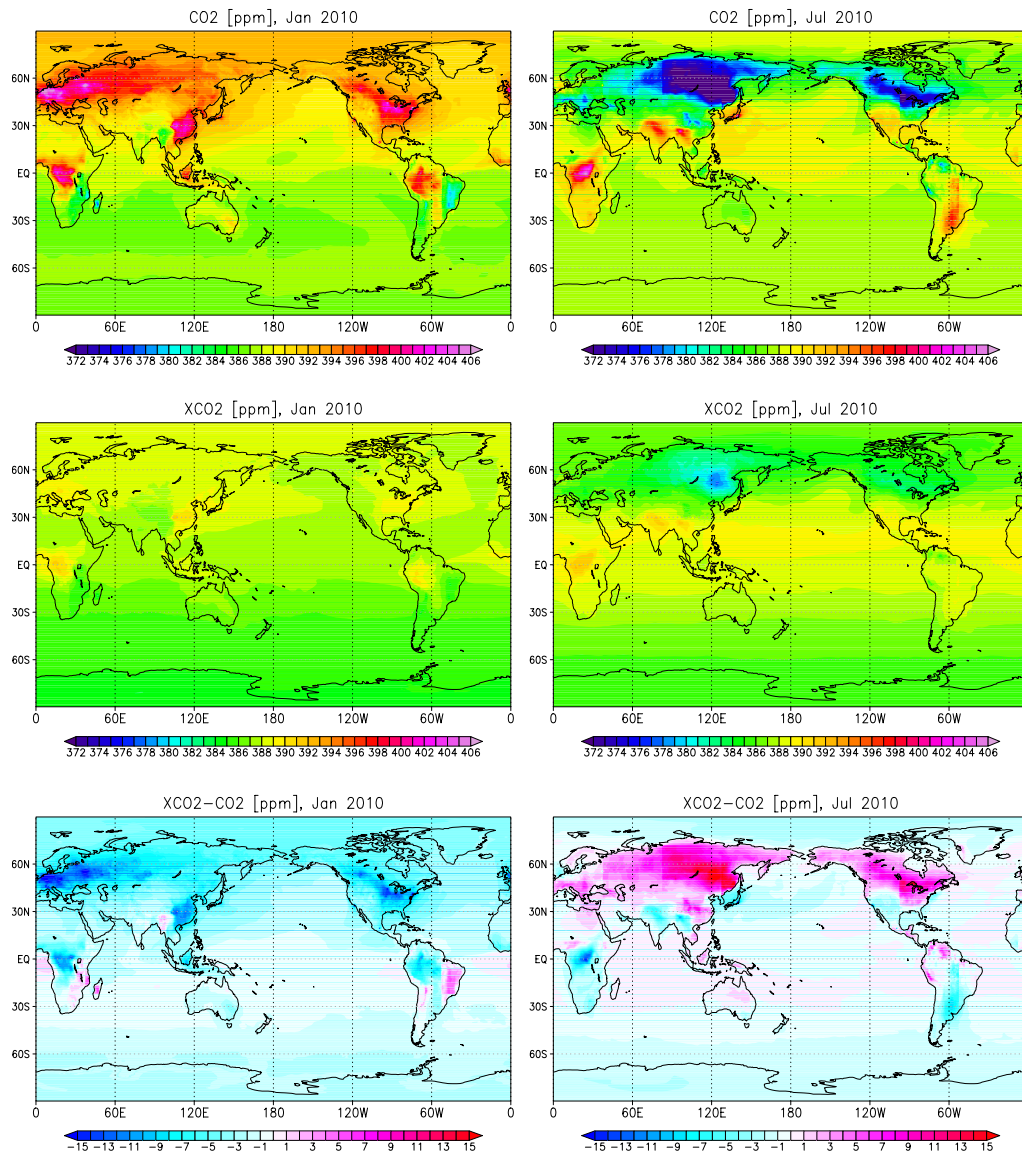


**Fig. 9.** Simulated monthly mean surface CO<sub>2</sub> (top), XCO<sub>2</sub> (middle) and their differences (bottom) at 13:00 LT in January (left column) and July (right column) 2010. Ranges of colour scales are 372–406 ppm for CO<sub>2</sub> and XCO<sub>2</sub>, and –15 to 15 ppm for the differences.

the upper tropopause and the model can capture such characteristics. While CO<sub>2</sub> is stable in the atmosphere, CH<sub>4</sub> reacts with O(<sup>1</sup>D) and Cl in the stratosphere in addition to chemical loss with OH radicals, creating a significant vertical decrease in the stratospheric concentration (Fig. 6). These atmospheric sinks for CH<sub>4</sub> create a negative difference in (XCH<sub>4</sub> – surface CH<sub>4</sub>) except for the equatorial region where the tropopause tends to be high due to strong convection.

Figure 11 shows the simulated surface CH<sub>4</sub> concentrations around Japan. The high-resolution model (0.5° × 0.5°; Fig. 11a) simulates a much clearer land–ocean contrast in CH<sub>4</sub> concentrations and synoptic-scale motions than the model with a resolution of 2° × 2° (Fig. 11b). An intrusion

of air mass with low CH<sub>4</sub> concentrations from the Pacific is more sharply resolved in the 0.5° simulation than at 2° resolution. The 0.5° model appears to be able to resolve point sources of CH<sub>4</sub>, such as highly populated urban areas (e.g., Tokyo), as shown by Maksyutov et al. (2008) for CO<sub>2</sub>.

Figure 12 shows monthly zonal-mean latitudinal distributions of surface CO<sub>2</sub> and XCO<sub>2</sub>, and their standard deviations at 13:00 LT, and Fig. 13 those of CH<sub>4</sub>. Zonal-mean surface CO<sub>2</sub> shows a strong sink centred on about 60° N in July, which then spreads toward high and low latitudes in August. The seasonal amplitude for XCO<sub>2</sub> is about 9 ppm, which is about half of that for surface CO<sub>2</sub>, 15 ppm. This tendency is consistent with previous modelling studies (e.g., Olsen and

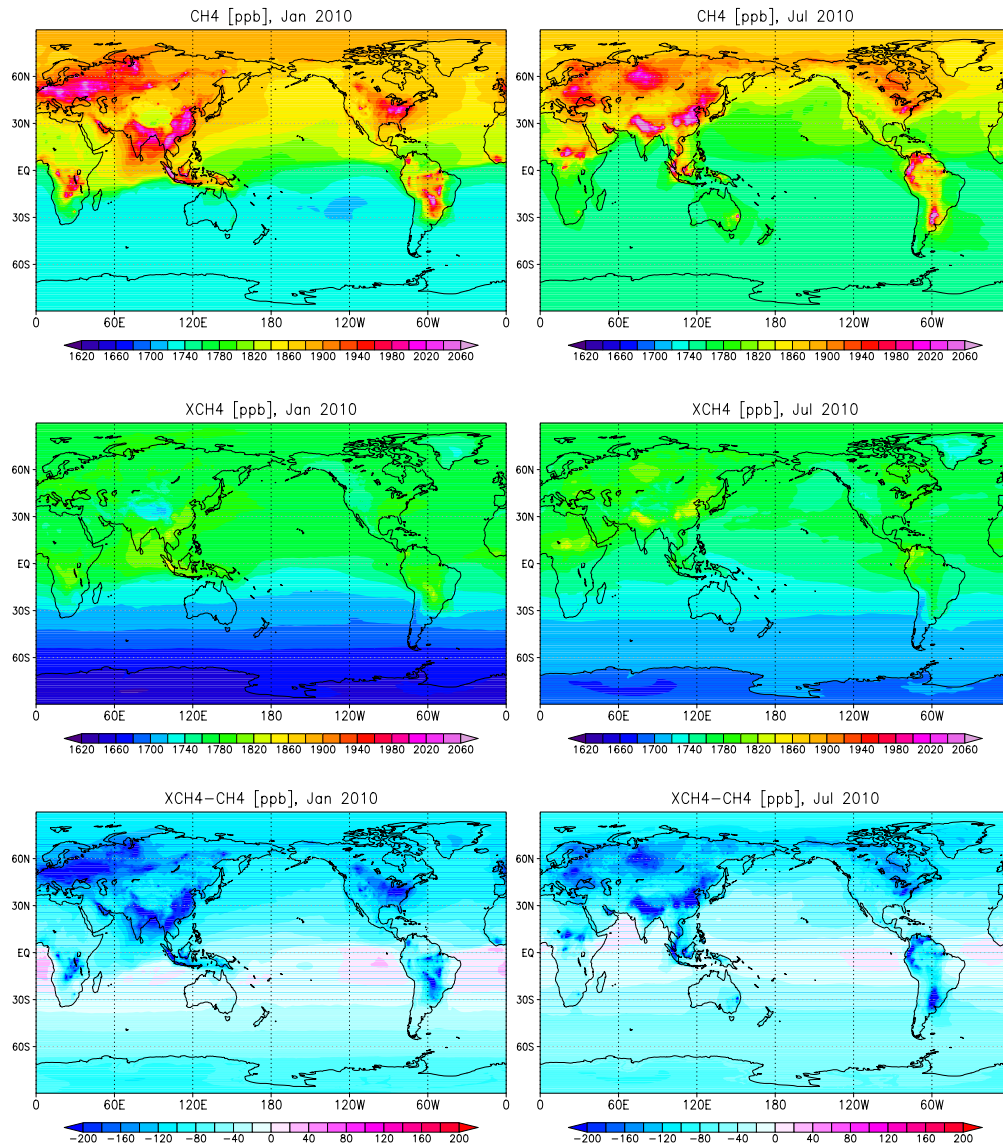


**Fig. 10.** Same as Fig. 7, but for CH<sub>4</sub>, XCH<sub>4</sub>, and their differences. Ranges of colour scales are 1620–2060 ppb for CH<sub>4</sub> and XCH<sub>4</sub>, and –200 to 200 ppb for the differences.

Randerson, 2004). Variances are large in northern mid and southern low latitudes, reflecting activity of land biosphere. The longitudinal variations in XCO<sub>2</sub> are about 2 ppm at maximum.

The north-to-south gradient of the concentrations modelled at the surface level and that of XCH<sub>4</sub> concentrations simulated at 13:00 LT were similar in trend; i.e., the concentrations in the Northern Hemisphere are higher than those in the Southern Hemisphere. XCH<sub>4</sub> values at every latitude are shifted to lower concentrations due to chemical OH loss in the tropopause and the stratosphere. Small peaks in XCH<sub>4</sub> are found in equatorial regions throughout the year, possibly

due to strong vertical transport of surface CH<sub>4</sub> by deep cumulus convection (e.g., Patra et al., 2009; Terao et al., 2011). CH<sub>4</sub> variance at the surface is high over most of the latitude band, reflecting the various CH<sub>4</sub> sources over land. This tendency is the same for XCH<sub>4</sub> but the variance is less than half the surface value. Relatively large variances in southern high latitudes might be due to the high elevation of the Antarctic Continent at over 3000 m, which makes this region susceptible to seasonal variations in tropopause height, as the stratospheric partial column of low CH<sub>4</sub> has a large weight.

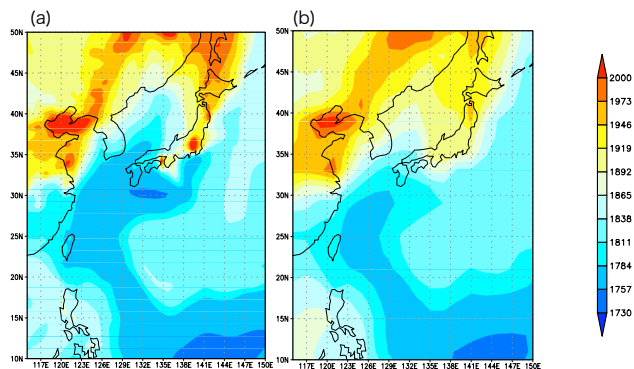


**Fig. 11.** Simulated surface CH<sub>4</sub> concentrations (ppb) around Japan at 13:00 JST on 6 July 2008 with a horizontal resolution of (a) 0.5° and (b) 2.0°.

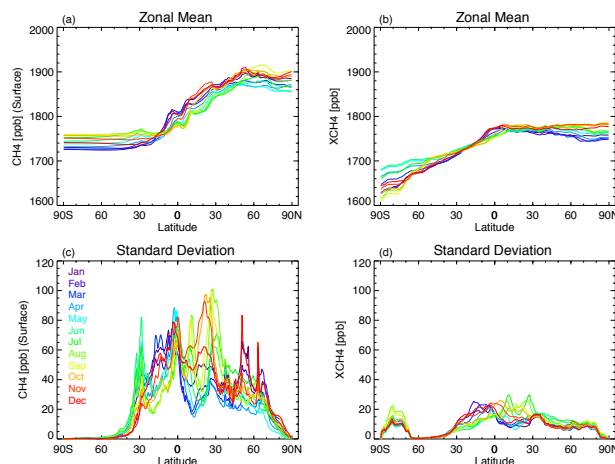


**Fig. 13.** Same as Fig. 11, but for CH<sub>4</sub> and XCH<sub>4</sub>.

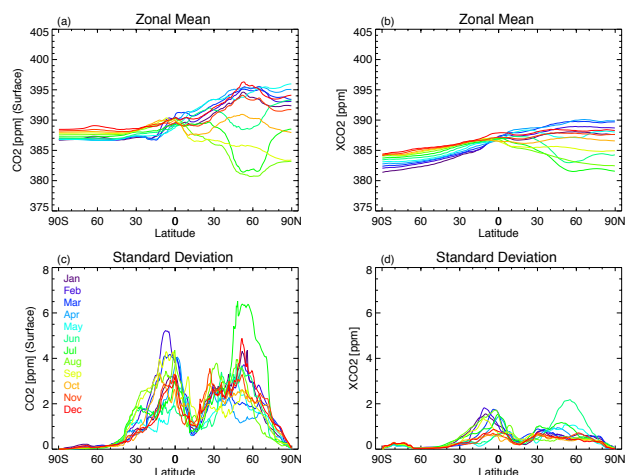


**Fig. 12.** Monthly zonal-mean latitudinal distributions of (a) CO<sub>2</sub> and (b) XCO<sub>2</sub> for 2010 and (c–d) their standard deviations against longitudinal variation.

## 4 Conclusions

We have developed the NIES transport model at a resolution of  $0.5^\circ \times 0.5^\circ \times 47$  sigma levels, driven by high-resolution meteorological data, GPV, with  $0.5^\circ \times 0.5^\circ$  resolution and 21 pressure levels (1000–10 hPa). This GPV-forced NIES TM has been designed to provide global high-resolution and near real-time a priori CO<sub>2</sub> and CH<sub>4</sub> concentrations for the GOSAT data retrieval algorithm to derive XCO<sub>2</sub> and XCH<sub>4</sub> at NIES. Since real-time fluxes of CO<sub>2</sub> and CH<sub>4</sub> are not available, the flux climatologies were used with the trend adjustment to the observed background concentrations. To overcome the problem of stratospheric transport in the model, the stratospheric part of the model was nudged to climatological values using three-dimensional CO<sub>2</sub> climatology that was adjusted to observed age of air for CO<sub>2</sub> and long-term satellite observations from HALOE for CH<sub>4</sub>. We also updated

the stratospheric part of the earlier version of a priori error variance–covariance matrices for CO<sub>2</sub> and CH<sub>4</sub> to give more realistic stratospheric values.

The model performance was assessed by comparing the model outputs with available observational records of atmospheric CO<sub>2</sub> and CH<sub>4</sub> concentrations. A large-scale, latitudinal distribution of the simulated annual mean CO<sub>2</sub> and CH<sub>4</sub> concentrations is found to be in good agreement with the analysis of GV sites, with overall annual biases and standard deviations of  $-0.25 \pm 1.47$  ppm and  $-0.31 \pm 12.57$  ppb, and with RMSDs of 1.45 ppm and 12.52 ppb at 155 CO<sub>2</sub> sites and 123 CH<sub>4</sub> sites, respectively. In particular, pole-to-pole gradients of CO<sub>2</sub> and CH<sub>4</sub> are reproduced exactly by the model with almost no biases. Comparison between monthly GV CO<sub>2</sub> and CH<sub>4</sub> and the model output showed that, despite large model–observation mismatch in monthly seasonal variations at some tower sites and some inland sites where large seasonal variations were observed, the model seasonal variations generally agreed well, particularly at oceanic and free tropospheric sites, with GV values with averaged correlation coefficients of 0.87 for CO<sub>2</sub> and 0.53 for CH<sub>4</sub> in terms of seasonal variations. The observed daily or discrete time series at MLO, SPO, HAT and COI are generally well reproduced by the model with statistically good performance, though some discrepancies were found, possibly due to the use of climatological fluxes. The synoptic variations at HAT and COI were reproduced better by the higher-resolution model (0.5°) than the coarser-resolution model (2.0°), that is, the correlation coefficients between the observation and the higher-resolution model were significantly higher than those for the lower-resolution model. In the stratosphere, the simulated vertical profiles and growth rates agree well with the average profiles from balloon-borne observations over Japan within the observed standard deviations. Overall the model biases are small enough compared to the current biases of

GOSAT Level 2 product (version 2.00) of XCO<sub>2</sub> and XCH<sub>4</sub>, thus, the model and the accompanied VCMs are appropriate for use in GOSAT Level 2 retrievals.

The global CO<sub>2</sub> and CH<sub>4</sub> distributions, and XCO<sub>2</sub> and XCH<sub>4</sub> obtained are in qualitative agreement with previous studies. The 0.5° model can resolve synoptic-scale motions and point sources better than the 2.0° model does. Seasonal amplitudes in zonal-mean XCO<sub>2</sub> are found to be almost half those for surface CO<sub>2</sub>. Zonal-mean XCH<sub>4</sub> shows different features from XCO<sub>2</sub> because of the chemical sinks in the atmosphere and its sensitivity to tropopause height.

These validations suggest that the model is able to reproduce fairly reasonable global concentrations as well as synoptic variations and give confidence in quantitative analysis of CO<sub>2</sub> and CH<sub>4</sub> cycles using the model, and its use in providing a priori concentrations for satellite retrievals. This model has been implemented on the GOSAT DHF system and has been run every observed day, and the simulated results have been used for a priori concentrations for GOSAT XCO<sub>2</sub> and XCH<sub>4</sub> retrievals. As future satellite instruments like OCO-2 are expected to have smaller footprints or higher precision to observe greenhouse gases more precisely, the ability to simulate a priori concentrations with a higher-resolution model would be useful in reducing error in a priori concentrations. Thus, the updated high-resolution concentrations and VCMs provided by the developed model have the potential to be powerful tools for a priori of satellite data retrievals as well as for the high-resolution global modelling of greenhouse gases.

## Appendix A

### A1 Mass fixer

The mass correction is distributed proportionally to local advection tendencies to conserve total tracer mass  $M_q$

$$M_q = \int_0^1 \int_{-1}^1 \int_0^{2\pi} p_s \cdot (1 - 0.61 \cdot q_w) \cdot q \cdot d\lambda \cdot d(\sin\phi) \cdot d\sigma \quad (\text{A1})$$

where  $p_s$  is surface pressure,  $q_w$  is mixing ratio of water vapour,  $\lambda$  and  $\phi$  indicate the position in the polar coordinate system. The mass fixer constrains tracer tendencies

$$\frac{\partial}{\partial t} M_q = 0 \quad (\text{A2})$$

on each time step. Hence, the corrected tendency  $\tilde{q}$  for each tracer is

$$\tilde{q} = \dot{q} \cdot [a_p \cdot \theta(\dot{q}) - a_n \cdot \theta(-\dot{q})] \quad (\text{A3})$$

where  $a_p$  and  $a_n$  are multipliers for positive and negative tendencies, and  $\theta(\dot{q})$  is the step function which  $\theta(x) = 1$  for  $x \geq 0$ , and  $\theta(x) = 0$  for  $x < 0$ . The condition  $\max(a_p, a_n)$  is enforced to keep the solution monotonic.

### A2 Cumulus convection

The cumulus convection is based on cumulus mass fluxes calculated in a Kuo-type scheme (Grell, 1995) and modified to include entrainment and detrainment processes on convective updrafts and downdrafts proposed by Tiedtke (1989).

First the cloud base level  $\sigma_c$  is calculated by adding small perturbation to humidity and temperature to levels below the  $\sigma$  level corresponding to 700 hPa and adiabatically lifting the air parcel until the condensation occurs. The cloud base  $\sigma_c$  is set to the lowest level where condensation would occur.

Then, we estimate the supply rate of moisture available for penetrative convection. The horizontal moisture divergence is evaluated from winds and water vapour content. Low-level moisture convergence is calculated by integrating the horizontal moisture convergence below cloud base level and the surface evaporation. The moisture divergence term is corrected for non-zero divergence of the air mass in order to take account for deviation from the mass conservation in the wind data.

The mass flux in updraft is set to low-level moisture convergence divided by water vapour mixing ratio at cloud base. The vertical profiles of entrainment and detrainment rates are set proportional to the updraft mass flux followed by Tiedtke (1989). In the updraft air, virtual potential temperatures are estimated from the cloud base level to cloud top level. The cloud top is determined by comparing the virtual potential temperatures in the updraft and environment, for which an overshoot of 3 degrees K is allowed.

The cloud with a thickness of thinner than  $\Delta\sigma = 0.1$  are excluded. The downdraft mass flux is set to 0.2 of that in the updraft, which is same as in Tiedtke (1989).

The tracers are transported vertically by applying a simplified explicit scheme. We assumed that the updrafts and downdrafts make only a negligibly small part of a grid column; the rest is designated as environment air. First the vertical profiles of the concentrations in the updraft and downdraft air are calculated by taking into account rates of mixing with environment air by entrainment and detrainment, and then the concentration tendencies in environment air are obtained from entrainment and detrainment rates.

### A3 Turbulent diffusion

Turbulent diffusion is temperature dependent (stability function) and is defined as follows: below PBL top, the turbulent diffusivity is set to constant value of  $40 \text{ m}^2 \text{ s}^{-1}$ , and above PBL, the turbulent diffusivity ( $K_T$ ) is calculated by using local stability function following Hack et al. (1993):

$$K_T = \ell^2 S F_s(Ri), \quad (\text{A4})$$

where  $\ell = 30 \text{ m}$  is mixing length,  $S = \left| \frac{\rho g}{P_s} \frac{\partial V}{\partial \sigma} \right|$  is the vertical wind shear,  $Ri$  is local Richardson number:

$$Ri = -\frac{\rho g^2}{P_s} \left( \frac{1}{S^2} \cdot \frac{\partial \ln \theta_V}{\partial \sigma} \right), \quad (A5)$$

which is a function of the virtual potential temperature ( $\theta_V$ ) and the acceleration of gravity ( $g$ ). Then stability dependent function  $F_s(Ri)$  is defined as:

$$\begin{aligned} F_s(Ri) &= (1 - 18 Ri)^{1/2} & (Ri < 0), \\ F_s(Ri) &= 1 - \frac{Ri}{Ri_c} & (0 < Ri < Ri_c = 0.2), \\ F_s(Ri) &= 0 & (Ri > Ri_c = 0.2). \end{aligned} \quad (A6)$$

#### A4 Model vertical sigma levels

The 47 vertical sigma levels of the model are defined as slab centres of slab interface below:

1.000, 0.996, 0.988, 0.978, 0.968, 0.955, 0.940, 0.920, 0.900, 0.875, 0.850, 0.825, 0.800, 0.775, 0.750, 0.725, 0.700, 0.675, 0.650, 0.625, 0.600, 0.575, 0.550, 0.525, 0.500, 0.475, 0.450, 0.425, 0.400, 0.375, 0.350, 0.325, 0.300, 0.275, 0.250, 0.225, 0.200, 0.175, 0.150, 0.125, 0.100, 0.085, 0.070, 0.060, 0.050, 0.040, 0.030, 0.020.

*Acknowledgements.* This study was supported by the GOSAT project at NIES. GOSAT is a joint project of the Japan Aerospace Exploration Agency (JAXA), the National Institute for Environmental Studies (NIES) and the Japanese Ministry of the Environment (MoE). The extended GPV dataset for the GOSAT project was provided by the Japan Meteorological Agency (JMA). We appreciate the NOAA ESRL GMD team for providing continuous data at MLO and SPO (PIs: Kirk Thoning for CO<sub>2</sub> data, Ed Dlugokencky for CH<sub>4</sub> data), T. Nakazawa and S. Aoki at Tohoku University for providing balloon-borne data, Y. Tohjima at CGER/NIES for providing CH<sub>4</sub> data at Hateruma and P. K. Patra at the Japan Agency for Marine–Earth Science and Technology for providing CH<sub>4</sub> flux data. We also thank T. Miyasaka at Fujitsu FIP Corporation for maintaining NIES TM in the GOSAT DHF. We are grateful to R. Law and an anonymous reviewer for useful comments to improve the manuscript. The numerical integrations were performed on the NIES Supercomputer System (NEC SX-8R/128M16).

Edited by: H. Garny

#### References

- Allen, M., Erickson, D., Kendall, W., Fu, J., Ott, L., and Pawson, S.: The influence of internal model variability in GEOS-5 on interhemispheric CO<sub>2</sub> exchange. *J. Geophys. Res.*, 117, D10107, doi:10.1029/2011JD017059, 2012.
- Aoki, S., Nakazawa, T., Machida, T., Sugawara, S., Morimoto, S., Hashida, G., Yamanouchi, T., Kawamura, K., and Honda, H.: Carbon dioxide variations in the stratosphere over Japan, Scandinavia and Antarctic. *Tellus B*, 55, 178–186, 2003.
- Belikov, D., Maksyutov, S., Miyasaka, T., Saeki, T., Zhuravlev, R., and Kiryushov, B.: Mass-conserving tracer transport modelling on a reduced latitude-longitude grid with NIES-TM. *Geosci. Model Dev.*, 4, 207–222, doi:10.5194/gmd-4-207-2011, 2011.
- Boesch, H., Baker, D., Connor, B. J., Crisp, D., and Miller, C.: Global Characterization of CO<sub>2</sub> Column Retrievals from Shortwave-Infrared Satellite Observations of the Orbiting Carbon Observatory-2 Mission. *Remote Sens.*, 3, 270–34, doi:10.3390/rs3020270, 2011.
- Brenkert, A. L.: Carbon dioxide emission estimates from fossil-fuel burning, hydraulic cement production, and gas flaring for 1995 on a one degree grid cell basis. Rep. NCP-058A, Carbon Dioxide Inf. Anal. Cent., Oak Ridge Natl. Lab., Oak Ridge, Tenn., available at: <http://cdiac.ornl.gov/epubs/ndp/ndp058a/ndp058a.html> (last access: 12 July 2012), 1998.
- Buchwitz, M., de Beek, R., Burrows, J. P., Bovensmann, H., Warneke, T., Notholt, J., Meirink, J. F., Goede, A. P. H., Bergamaschi, P., Körner, S., Heimann, M., and Schulz, A.: Atmospheric methane and carbon dioxide from SCIAMACHY satellite data: initial comparison with chemistry and transport models. *Atmos. Chem. Phys.*, 5, 941–962, doi:10.5194/acp-5-941-2005, 2005.
- Butz, A., Guerlet, S., Hasekamp, O., Schepers, D., Galli, A., Aben, I., Frankenberg, C., Hartmann, J.-M., Tran, H., Kuze, A., Keppel-Aleks, G., Toon, G., Wunch, D., Wennberg, P., Deutscher, N., Griffith, D., Macatangay, R., Messerschmidt, J., Notholt, J., and Warneke, T.: Toward accurate CO<sub>2</sub> and CH<sub>4</sub> observations from GOSAT. *Geophys. Res. Lett.*, 38, L14812, doi:10.1029/2011GL047888, 2011.
- Connor, B. J., Boesch, H., Toon, G., Sen, B., Miller, C., and Crisp, D.: Orbiting Carbon Observatory: Inverse method and prospective error analysis. *J. Geophys. Res.*, 113, D05305, doi:10.1029/2006JD008336, 2008.
- De Mazière, M., Vigouroux, C., Bernath, P. F., Baron, P., Blumenstock, T., Boone, C., Brogniez, C., Catoire, V., Coffey, M., Duchatelet, P., Griffith, D., Hannigan, J., Kasai, Y., Kramer, I., Jones, N., Mahieu, E., Manney, G. L., Piccolo, C., Randall, C., Robert, C., Senten, C., Strong, K., Taylor, J., Tétard, C., Walker, K. A., and Wood, S.: Validation of ACE–FTS v2.2 methane profiles from the upper troposphere to the lower mesosphere. *Atmos. Chem. Phys.*, 8, 2421–2435, doi:10.5194/acp-8-2421-2008, 2008.
- Dlugokencky, E. J.: Atmospheric CH<sub>4</sub> daily mean data, Mauna Loa, World Data Center for Greenhouse Gases, Japan Meteorol. Agency, Tokyo, available at: <http://ds.data.jma.go.jp/gmd/wdcgg/wdcgg.html> (last access: 12 July 2012), 2012a.
- Dlugokencky, E. J.: Atmospheric CH<sub>4</sub> daily mean data, South Pole, World Data Center for Greenhouse Gases, Japan Meteorol. Agency, Tokyo, available at: <http://ds.data.jma.go.jp/gmd/wdcgg/wdcgg.html> (last access: 12 July 2012), 2012b.
- Dlugokencky, E. J., Harris, J. M., Chung, Y. S., Tans, P. P., and Fung, I.: The relationship between the methane seasonal cycle and regional sources and sinks at Tae-ahn Peninsula, Korea. *Atmos. Environ.*, 27, 2115–2120, 1993.
- Eguchi, N., Saito, R., Saeki, T., Nakatsuka, Y., Belikov, D., and Maksyutov, S.: A priori covariance estimation for CO<sub>2</sub> and CH<sub>4</sub> retrievals. *J. Geophys. Res.*, 115, D10215, doi:10.1029/2009JD013269, 2010.
- Engel, A., Möbius, T., Bönisch, H., Schmidt, U., Heinz, R., Levin, I., Atlas, E., Aoki, S., Nakazawa, T., Sugawara, S., Moore, F.,

- Hurst, D., Elkins, J., Schauffler, S., Andrews, A., and Boering, K.: Age of stratospheric air unchanged within uncertainties over the past 30 years, *Nat. Geosci.*, 2, 28–31, doi:10.1038/ngeo388, 2009.
- Fung, I., John, J., Lerner, J., Matthews, E., Prather, M., Steele, L. P., and Fraser, P. J.: Three-dimensional model synthesis of the global methane cycle, *J. Geophys. Res.*, 96, 13033–13065, 1991.
- Geels, C., Doney, S., Dargaville, R., Brandt, J., and Christensen, J. H.: Investigating the sources of synoptic variability in atmospheric CO<sub>2</sub> measurements over the Northern Hemisphere continents: A regional model study, *Tellus B*, 56, 35–50, 2004.
- Geels, C., Gloor, M., Ciais, P., Bousquet, P., Peylin, P., Vermeulen, A. T., Dargaville, R., Aalto, T., Brandt, J., Christensen, J. H., Frohn, L. M., Haszpra, L., Karstens, U., Rödenbeck, C., Ramonet, M., Carboni, G., and Santaguida, R.: Comparing atmospheric transport models for future regional inversions over Europe – Part 1: mapping the atmospheric CO<sub>2</sub> signals, *Atmos. Chem. Phys.*, 7, 3461–3479, doi:10.5194/acp-7-3461-2007, 2007.
- GLOBALVIEW-CH<sub>4</sub>: Cooperative Atmospheric Data Integration Project – Methane, CD-ROM, NOAA/CMDL, Boulder, Colorado, available via anonymous FTP to ftp.cmdl.noaa.gov, Path: ccg/ch4/GLOBALVIEW, 2009.
- GLOBALVIEW-CO<sub>2</sub>: Cooperative Atmospheric Data Integration Project – Carbon Dioxide, CD-ROM, NOAA/CMDL, Boulder, Colorado, available via anonymous FTP to ftp.cmdl.noaa.gov, Path: ccg/co2/GLOBALVIEW, 2009.
- Grell, G., Dudhia, J., and Stauffer, D.: Description of the Fifth-Generation Penn State/NCAR Mesoscale Model (MM5), NCAR/TN-398, NCAR, Boulder, Colo., USA, 1995.
- Gurney, K. R., Law, R. M., Denning, A. S., Rayner, P. J., Baker, D., Bousquet, P., Bruhwiler, L., Chen, Y.-H., Ciais, P., Fan, S., Fung, I. Y., Gloor, M., Heimann, M., Higuchi, K., John, J., Maki, T., Maksyutov, S., Masarie, K., Peylin, P., Prather, M., Pak, B. C., Randerson, J., Sarmiento, J., Taguchi, S., Takahashi, T., and Yuen, C.-W.: Towards robust regional estimates of CO<sub>2</sub> sources and sinks using atmospheric transport models, *Nature*, 415, 626–630, 2002.
- Gurney, K. R., Denning, A. S., Rayner, P., Pak, B., Baker, D., Bousquet, P., Bruhwiler, L., Chen, Y.-H., Ciais, P., Fung, I. Y., Heimann, M., Higuchi, K., John, J., Maki, T., Maksyutov, S., Peylin, P., Prather, M., and Taguchi, S.: Transcom 3 inversion intercomparison: Model mean results for the estimation of seasonal carbon sources and sinks, *Global Biogeochem. Cy.*, 18, GB1010, doi:10.1029/2003GB002111, 2004.
- Hack, J. J., Boville, B. A., Briegleb, B. P., Kiehl, J. T., Rasch, P. J., and Williamson, D. L.: Description of the NCAR community climate model (CCM2), NCAR/TN-382, NCAR, Boulder, Colo., USA, 1993.
- Higuchi, K., Murayama, S., and Taguchi, S.: Quasi-decadal variation of the atmospheric CO<sub>2</sub> seasonal cycle due to atmospheric circulation changes: 1979–1998, *Geophys. Res. Lett.*, 29, 1173, doi:10.1029/2001GL013751, 2002.
- Japan Aerospace Exploration Agency: National Institute for Environmental Studies, and Ministry of the Environment, GOSAT/IBUKI Data Users Handbook, 1st Edn., available at: [https://data.gosat.nies.go.jp/GosatUserInterfaceGateway/guig/doc/GOSAT\\_HB\\_E\\_1stEdition\\_for\\_HP.pdf](https://data.gosat.nies.go.jp/GosatUserInterfaceGateway/guig/doc/GOSAT_HB_E_1stEdition_for_HP.pdf) (last access: 12 July 2012), 2011.
- JMA: Outline of the operational numerical weather prediction at the Japan Meteorological Agency. (Appendix to the WMO Technical Progress Report on the Global Data-Processing and Forecasting System and Numerical Weather Prediction), Japan Meteorological Agency, 194, available at: <http://www.jma.go.jp/jma/jma-eng/jma-center/nwp/outline-nwp/index.htm> (last access: 12 July 2012), 2007.
- Kuze, A., Suto, H., Nakajima, M., and Hamazaki, T.: Thermal and near infrared sensor for carbon observation Fourier-transform spectrometer on the Greenhouse Gases Observing Satellite for greenhouse gases monitoring, *Appl. Optics*, 48, 6716–6733, 2009.
- Law, R. M., Peters, W., Rödenbeck, C., Aulagnier, C., Baker, I., Bergmann, D. J., Bousquet, P., Brandt, J., Bruhwiler, L., Cameron-Smith, P. J., Christensen, J. H., Delage, F., Denning, A. S., Fan, S., Geels, C., Houweling, S., Imasu, R., Karstens, U., Kawa, S. R., Kleist, J., Krol, M. C., Lin, S. J., Lokupitiya, R., Maki, T., Maksyutov, S., Niwa, Y., Onishi, R., Parazoo, N., Patra, P. K., Pieterse, G., Rivier, L., Satoh, S., Serrar, S., Taguchi, S., Takigawa, M., Vautard, R., Vermeulen, A. T., and Zhu, Z.: TransCom model simulations of hourly atmospheric CO<sub>2</sub>: Experimental overview and diurnal cycle results for 2002, *Global Biogeochem. Cy.*, 22, GB3009, doi:10.1029/2007GB003050, 2008.
- Maksyutov, S., Patra, P. K., Onishi, R., Saeki, T., and Nakazawa, T.: NIES/FRCGC global atmospheric tracer transport model: Description, validation, and surface sources and sinks inversion, *J. Earth Simulator*, 9, 3–18, 2008.
- Masarie, K. and Tans, P. P.: Extension and integration of atmospheric carbon dioxide data into a globally consistent measurement record, *J. Geophys. Res.*, 100, 11593–11610, doi:10.1029/95JD00859, 1995.
- Nakazawa, T., Morimoto, S., Aoki, S., and Tanaka, M.: Time and space variations of the carbon isotopic ratio of the tropospheric carbon dioxide over Japan, *Tellus B*, 45, 258–274, 1993.
- Nakazawa, T., Ishizawa, M., Higuchi, K., and Trivett, N.: Two curve fitting methods applied to CO<sub>2</sub> flask data, *Environmetrics*, 8, 197–218, 1997.
- Nakazawa, T., Aoki, S., Kawamura, K., Saeki, T., Sugawara, S., Honda, H., Hashida, G., Morimoto, S., Yoshida, N., Toyoda, S., Makide, Y., and Shirai, T.: Variations of stratospheric trace gases measured using a balloon-borne cryogenic sampler, *Adv. Space Res.*, 30, 1349–1357, 2002.
- NIES GOSAT Project: Summary of the GOSAT Level 2 Data Product Validation Activity, available at: [https://data.gosat.nies.go.jp/GosatWebDds/productorder/distribution/user/ValidationResult\\_FTSSWIRL2\\_V02.xx\\_GU\\_en.pdf](https://data.gosat.nies.go.jp/GosatWebDds/productorder/distribution/user/ValidationResult_FTSSWIRL2_V02.xx_GU_en.pdf) (last access: 12 July 2012), 2012.
- O'Dell, C. W., Connor, B., Bösch, H., O'Brien, D., Frankenberg, C., Castano, R., Christi, M., Eldering, D., Fisher, B., Gunson, M., McDuffie, J., Miller, C. E., Natraj, V., Oyafuso, F., Polonsky, I., Smyth, M., Taylor, T., Toon, G. C., Wennberg, P. O., and Wunch, D.: The ACOS CO<sub>2</sub> retrieval algorithm – Part 1: Description and validation against synthetic observations, *Atmos. Meas. Tech.*, 5, 99–121, doi:10.5194/amt-5-99-2012, 2012.
- Olivier, J. G. J. and Berdowski, J. J. M.: Global emissions sources and sinks, in: *The Climate System*, A. A. Balkema Publishers/Swets and Zeitlinger Publishers, Lisse, The Netherlands, 33–78, 2001.

- Olsen, S. C. and Randerson, J. T.: Differences between surface and column atmospheric CO<sub>2</sub> and implications for carbon cycle research, *J. Geophys. Res.*, 109, D02301, doi:10.1029/2003JD003968, 2004.
- Oshchepkov, S., Bril, A., Maksyutov, S., and Yokota, T.: Detection of optical path in spectroscopic space-based observations of greenhouse gases: Application to GOSAT data processing, *J. Geophys. Res.*, 116, D14304, doi:10.1029/2010JD015352, 2011.
- Park, J. H., Russell III, J. M., Gordley, L. L., Drayson, S. R., Benner, D. C., McInerney, J. M., Gunson, M. R., Toon, G. C., Sen, B., Blavier, J.-F., Webster, C. R., Zipf, E. C., Erdman, P., Schmidt, U., and Schiller, C.: Validation of Halogen Occultation Experiment CH<sub>4</sub> measurements from the UARS, *J. Geophys. Res.*, 101, 10183–10203, doi:10.1029/95JD02736, 1996.
- Patra, P. K. and Maksyutov, S.: Incremental approach to the optimal network design for CO<sub>2</sub> surface source inversion, *Geophys. Res. Lett.*, 29, 1459, doi:10.1029/2001GL013943, 2002.
- Patra, P. K., Maksyutov, S., Sasano, Y., Nakajima, H., Inoue, G., and Nakazawa, T.: An evaluation of CO<sub>2</sub> observations with Solar Occultation FTS for Inclined-Orbit Satellite sensor for surface source inversion, *J. Geophys. Res.*, 108, 4759, doi:10.1029/2003JD003661, 2003.
- Patra, P. K., Ishizawa, M., Maksyutov, S., Nakazawa, T., and Inoue, G.: Role of biomass burning and climate anomalies for land-atmosphere carbon fluxes based on inverse modeling of atmospheric CO<sub>2</sub>, *Global Biogeochem. Cy.*, 19, GB3005, doi:10.1029/2004GB002258, 2005a.
- Patra, P. K., Maksyutov, S., and Nakazawa, T.: Analysis of atmospheric CO<sub>2</sub> growth rates at Mauna Loa using inverse model derived CO<sub>2</sub> fluxes, *Tellus B*, 57, 357–365, 2005b.
- Patra, P. K., Law, R. M., Peters, W., Rödenbeck, C., Takigawa, M., Aulagnier, C., Baker, I., Bergmann, D. J., Bousquet, P., Brandt, J., Bruhwiler, L., Cameron-Smith, P. J., Christensen, J. H., Delage, F., Denning, A. S., Fan, S., Geels, C., Houweling, S., Imasu, R., Karstens, U., Kawa, S. R., Kleist, J., Krol, M. C., Lin, S.-J., Lokupitiya, R., Maki, T., Maksyutov, S., Niwa, Y., Onishi, R., Parazoo, N., Pieterse, G., Rivier, L., Satoh, M., Serrar, S., Taguchi, S., Vautard, R., Vermeulen, A. T., and Zhu, Z.: TransCom model simulations of hourly atmospheric CO<sub>2</sub>: Analysis of synoptic-scale variations for the period 2002–2003, *Global Biogeochem. Cy.*, 22, GB4013, doi:10.1029/2007GB003081, 2008.
- Patra, P. K., Takigawa, M., Ishijima, K., Choi, B.-C., Cunnold, D., Dlugokencky, E. J., Fraser, P., Gomez-Pelaez, A. J., Goo, T.-Y., Kim, J.-S., Krummel, P., Langenfelds, R., Meinhardt, F., Mukai, H., O'Doherty, S., Prinn, R. G., Simmonds, P., Steele, P., Tohjima, Y., Tsuboi, K., Uhse, K., Weiss, R., Worthy, D., and Nakazawa, T.: Growth rate, seasonal, synoptic and diurnal variations in lower atmospheric methane and its budget, *J. Meteorol. Soc. Jpn.*, 87, 635–663, 2009.
- Patra, P. K., Houweling, S., Krol, M., Bousquet, P., Belikov, D., Bergmann, D., Bian, H., Cameron-Smith, P., Chipperfield, M. P., Corbin, K., Fortems-Cheiney, A., Fraser, A., Gloor, E., Hess, P., Ito, A., Kawa, S. R., Law, R. M., Loh, Z., Maksyutov, S., Meng, L., Palmer, P. I., Prinn, R. G., Rigby, M., Saito, R., and Wilson, C.: TransCom model simulations of CH<sub>4</sub> and related species: linking transport, surface flux and chemical loss with CH<sub>4</sub> variability in the troposphere and lower stratosphere, *Atmos. Chem. Phys.*, 11, 12813–12837, doi:10.5194/acp-11-12813-2011, 2011.
- Pérez-Landa, G., Ciais, P., Sanz, M. J., Gioli, B., Miglietta, F., Palau, J. L., Gangoiti, G., and Millán, M. M.: Mesoscale circulations over complex terrain in the Valencia coastal region, Spain – Part 1: Simulation of diurnal circulation regimes, *Atmos. Chem. Phys.*, 7, 1835–1849, doi:10.5194/acp-7-1835-2007, 2007a.
- Pérez-Landa, G., Ciais, P., Gangoiti, G., Palau, J. L., Carrara, A., Gioli, B., Miglietta, F., Schumacher, M., Millan, M. M., and Sanz, M. J.: Mesoscale circulations over complex terrain in the Valencia coastal region, Spain – Part 2: Modeling CO<sub>2</sub> transport using idealized surface fluxes, *Atmos. Chem. Phys.*, 7, 1851–1868, doi:10.5194/acp-7-1851-2007, 2007b.
- Randerson, J. T., Thompson, M. V., Conway, T. J., Fung, I. Y., and Field, C. B.: The contribution of terrestrial sources and sinks to trends in the seasonal cycle of atmospheric carbon dioxide, *Global Biogeochem. Cy.*, 11, 535–560, 1997.
- Reuter, M., Bovensmann, H., Buchwitz, M., Burrows, J. P., Connor, B. J., Deutscher, N. M., Griffith, D. W. T., Heymann, J., Keppel-Aleks, G., Messerschmidt, J., Notholt, J., Petri, C., Robinson, J., Schneising, O., Sherlock, V., Velasco, V., Warneke, T., Wennberg, P. O., and Wunch, D.: Retrieval of atmospheric CO<sub>2</sub> with enhanced accuracy and precision from SCIAMACHY: Validation with FTS measurements and comparison with model results, *J. Geophys. Res.*, 116, D04301, doi:10.1029/2010JD015047, 2011.
- Rodgers, C. D.: Characterization and error analysis of profiles retrieved from remote sounding measurements, *J. Geophys. Res.*, 95, 5587–5595, 1990.
- Russell III, J. M., Gordley, L. L., Park, J. H., Drayson, S. R., Hesketh, D. H., Cicerone, R. J., Tuck, A. F., Frederick, J. E., Harries, J. E., and Crutzen, P. J.: The Halogen Occultation Experiment, *J. Geophys. Res.*, 98, 10777–10797, 1993.
- Saito, R., Houweling, S., Patra, P. K., Belikov, D., Lokupitiya, R., Niwa, Y., Chevallier, F., Saeki, T., and Maksyutov, S.: TransCom satellite intercomparison experiment: Construction of a bias corrected atmospheric CO<sub>2</sub> climatology, *J. Geophys. Res.*, 116, D21120, doi:10.1029/2011JD016033, 2011.
- Saitoh, N., Imasu, R., Ota, Y., and Niwa, Y.: CO<sub>2</sub> retrieval algorithm for the thermal infrared spectra of the Greenhouse Gases Observing Satellite: Potential of retrieving CO<sub>2</sub> vertical profile from high-resolution FTS sensor, *J. Geophys. Res.*, 114, D17305, doi:10.1029/2008JD011500, 2009.
- Schepers, D., Guerlet, S., Butz, A., Landgraf, J., Frankenberg, C., Hasekamp, O., Blavier, J.-F., Deutscher, N. M., Griffith, D. W. T., Hase, F., Kyro, E., Morino, I., Sherlock, V., Sussmann, R., and Aben, I.: Methane retrievals from Greenhouse Gases Observing Satellite (GOSAT) shortwave infrared measurements: Performance comparison of proxy and physics retrieval algorithms, *J. Geophys. Res.*, 117, D10307, doi:10.1029/2012JD017549, 2012.
- Spivakovskiy, C. M., Logan, J. A., Montzka, S. A., Balkanski, Y. J., Foreman-Fowler, M., Jones, D. B. A., Horowitz, L. W., Fusco, A. C., Brenninkmeijer, C. A. M., Prather, M. J., Wofsy, S. C., and McElroy, M. B.: Three dimensional climatological distribution of tropospheric OH: Update and evaluation, *J. Geophys. Res.*, 105, 8931–8980, 2000.
- Takahashi, T., Sutherland, S. C., Sweeney, C., Poisson, A., Metzler, N., Tilbrook, B., Bates, N., Wanninkhof, R., Feely, R. A., Sabine, C., Olafsson, J., and Nojiri, Y.: Global sea-air CO<sub>2</sub> flux based on climatological surface ocean pCO<sub>2</sub>, and seasonal biological and temperature effects, *Deep Sea Res. Part II*, 49, 1601–1622, 2002.

- Terao, Y., Mukai, H., Nojiri, Y., Machida, T., Tohjima, Y., Saeki, T., and Maksyutov, S.: Interannual variability and trends in atmospheric methane over the western Pacific from 1994 to 2010, *J. Geophys. Res.*, 116, D14303, doi:10.1029/2010JD015467, 2011.
- Thoning, K. W.: Atmospheric CO<sub>2</sub> daily mean data, Mauna Loa, World Data Center for Greenhouse Gases, Japan Meteorol. Agency, Tokyo, available at: <http://ds.data.jma.go.jp/gmd/wdcgg/wdcgg.html> (last access: 12 July 2012), 2012a.
- Thoning, K. W.: Atmospheric CO<sub>2</sub> daily mean data, South Pole, World Data Center for Greenhouse Gases, Japan Meteorol. Agency, Tokyo, available at: <http://ds.data.jma.go.jp/gmd/wdcgg/wdcgg.html> (last access: 12 July 2012), 2012b.
- Tiedtke, M.: A comprehensive mass flux scheme for cumulus parameterization in large-scale models, *Mon. Weather Rev.*, 117, 1779–1800, 1989.
- Tohjima, Y., Machida, T., Utiyama, M., Katsumoto, M., Fujinuma, Y., and Maksyutov, S.: Analysis and presentation of in situ atmospheric methane measurements from Cape Ochi-ishi and Hateruma Island, *J. Geophys. Res.*, 107, 4148, doi:10.1029/2001JD001003, 2002.
- Tohjima, Y., Mukai, H., Hashimoto, S., and Patra, P. K.: Increasing synoptic scale variability in atmospheric CO<sub>2</sub> at Hateruma Island associated with increasing East-Asian emissions, *Atmos. Chem. Phys.*, 10, 453–462, doi:10.5194/acp-10-453-2010, 2010.
- Wang, J.-W., Denning, A. S., Lu, L., Baker, I. T., Corbin, K. D., and Davis, K. J.: Observations and simulations of synoptic, regional, and local variations in atmospheric CO<sub>2</sub>, *J. Geophys. Res.*, 112, D04108, doi:10.1029/2006JD007410, 2007.
- Washenfelder, R. A., Wennberg, P. O., and Toon, G. C.: Tropospheric methane retrieved from ground-based near-IR solar absorption spectra, *Geophys. Res. Lett.*, 30, 2226, doi:10.1029/2003GL017969, 2003.
- Xiong, X., Houweling, S., Wei, J., Maddy, E., Sun, F., and Barnet, C.: Methane plume over south Asia during the monsoon season: satellite observation and model simulation, *Atmos. Chem. Phys.*, 9, 783–794, doi:10.5194/acp-9-783-2009, 2009.
- Yokota, Y., Yoshida, Y., Eguchi, N., Ota, Y., Tanaka, T., Watanabe, H., and Maksyutov, S.: Global Concentrations of CO<sub>2</sub> and CH<sub>4</sub> Retrieved from GOSAT: First Preliminary Results, *SOLA*, 5, 160–163, doi:10.2151/sola.2009-041, 2009.
- Yoshida, Y., Ota, Y., Eguchi, N., Kikuchi, N., Nobuta, K., Tran, H., Morino, I., and Yokota, T.: Retrieval algorithm for CO<sub>2</sub> and CH<sub>4</sub> column abundances from short-wavelength infrared spectral observations by the Greenhouse gases observing satellite, *Atmos. Meas. Tech.*, 4, 717–734, doi:10.5194/amt-4-717-2011, 2011.
- Yoshida, Y., Kikuchi, N., Morino, I., Uchino, O., Oshchepkov, S., Bril, A., Saeki, T., Schutgens, N., Toon, G. C., Wunch, D., Roehl, C. M., Wennberg, P. O., Griffith, D. W. T., Deutscher, N. M., Warneke, T., Notholt, J., Robinson, J., Sherlock, V., Connor, B., Rettinger, M., Sussmann, R., Ahonen, P., Heikkinen, P., Kyrö, E., and Yokota, T.: Improvement of the retrieval algorithm for GOSAT SWIR XCO<sub>2</sub> and XCH<sub>4</sub> and their validation using TC-CON data, *Atmos. Meas. Tech. Discuss.*, submitted, 2013.